

Institut für Angewandte Photophysik,
Fachrichtung Physik,
Fakultät Mathematik und Naturwissenschaften,
Technische Universität Dresden.

Polarisation splitting, moderadius and spatial mode locking in planar organic DBR microcavities.

Diplomarbeit
zur Erlangung des akademischen Grades
Diplom-Physiker.

Vorgelegt von: Felix Becker
geboren am: 03. August 1984 in Leipzig.

Dresden, 2009.

1. Gutachter: Prof. Dr. Karl Leo.
2. Gutachter: Prof. Dr. Roland Sauerbrey.

Eingereicht am 30. November 2009.

Abstract.

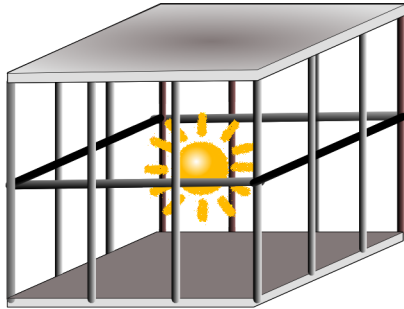
This work presents studies on the angle and mode tuning dependencies of the polarisation splitting in detuned organic DBR microcavities. The cavity layer has a wedged shape. By varying the measurement position on the sample, the resonant cavity mode is spectrally shifted with respect to the centre of the cavity stop band. For the first time, direct measurements of the dependence of the cavity mode polarisation splitting on mode tuning are carried out. Splitting values up to 58 meV are observed, where the resonant modes reach the stop band edge. This behaviour is compared with transfer matrix calculations and analytical considerations, which agree well.

In a second part, considerations about the radius of the resonant modes of organic DBR microcavities are presented, and the effects of mode growing and spatial mode locking in the laser regime are studied. The sample is excited with two small spots which are a few μm apart. It is found that photons from one spot can stimulate emission in the other spot, so that the phase of the emission from both spots locks in and a supermode forms, resulting in overall coherent emission. The phase difference between both spots is found to be either 0 or π , depending on the spot distance, resulting in normal or oblique laser emission.

Zusammenfassung.

Diese Arbeit stellt Untersuchungen über die Abhängigkeit der Polarisationsaufspaltung der Moden dielektrischer organischer Mikroresonatoren vom Winkel und der Modenstimmung vor. Die Resonatorschicht besitzt Keilform. Durch Veränderung der Messposition auf der Probe wird die resonante Kavitätsmode im Vergleich zur Mitte des Resonatorstopbandes spektral verschoben. Erstmals wird die Abhängigkeit der Polarisationsaufspaltung von der Modenabstimmung direkt gemessen. Es werden Aufspaltungen bis zu 58 meV beobachtet, wenn die Kavitätsmode den Rand des Stoppbandes erreicht. Dieses Verhalten wird mit Transfermatrixrechnungen und analytischen Betrachtungen verglichen, und die Ergebnisse stimmen überein.

In einem zweiten Teil werden Betrachtungen über den Radius der Resonatormoden vorgestellt. Der Effekt des Anwachsens der Moden und der räumlichen Modenkopplung im Laserregime werden untersucht. Die Probe wird an zwei Orten, welche wenige μm auseinanderliegen, angeregt. Es wird beobachtet, dass Photonen, die an der einen Stelle emittiert werden, Emission am anderen Ort stimulieren können, so dass die Phase der Emission von beiden Stellen einrastet und eine Supermode entsteht, was kohärente Abstrahlung von beiden Orten bewirkt. Die Phasendifferenz zwischen beiden angeregten Stellen ist entweder 0 oder π , abhängig von deren Abstand, was zu Emission in senkrechter oder schräger Richtung führt.



„In unserem Rathaus ist es finster!“ „Stimmt!“ riefen die anderen. Als aber der Bäcker fragte: „Und woran liegt das?“, wussten sie lange keine Antwort. Bis der Schneider schüchtern sagte: „Ich glaube, ich hab’s.“ „Nun?“ „In unserm neuen Rathaus“, fuhr der Schneider bedächtig fort, „ist kein Licht!“ Da sperrten sie Mund und Nase auf und nickten zwanzigmal. Der Schneider hatte Recht, Im Rathaus war es finster, weil kein Licht drin war!

Am Abend trafen sie sich beim Ochsenwirt, tranken ein Bier und beratschlagten, wie man Licht ins Rathaus hineinschaffen könne. Es wurden eine ganze Reihe Vorschläge gemacht. Doch sie gefielen ihnen nicht besonders. Erst nach dem fünften Glas Braunbier fiel dem Hufschmied das Richtige ein. „Das Licht ist lebendig wie ein Kaninchen“, sagte er nachdenklich. „Und da man Kaninchen in Käfigen ins Haus trägt, sollten wir’s mit dem Licht genauso machen!“

„Hurra!“, riefen sie alle. „Das ist die Lösung!“

(Frei aus die Schildbürger [1].)

Contents.

1	Introduction.	7
2	Theoretical Basis.	10
2.1	Ways of describing Light.	10
2.2	Stimulated Emission and Lasing.	11
2.2.1	Photon Emission Processes.	12
2.2.2	Light Amplification, Gain and Laser Threshold.	13
2.2.3	Emission in optical Resonators and Purcell Effect.	16
2.3	Review of the Fresnel Formulae.	17
2.4	Review of Transfer Matrix Calculations.	20
2.5	Dielectric Bragg Reflectors (DBRs).	24
2.6	DBR Microcavities and Polarisation Properties.	26
2.6.1	Introduction to DBR microcavities.	26
2.6.2	Modes of DBR microcavities.	29
2.6.3	Polarisation splitting in DBR microcavities.	32
2.6.4	Electromagnetic field enhancement in microcavities.	33
2.7	Fabry-Pérot Interferometer. Angular Dependent Cavity Transmission Spectrum.	34
2.8	Effective Reflectance.	37
2.9	Cavity Mode Radius.	39
2.10	Spatial Mode Locking.	44
3	Experimental Setup.	46
4	Measurement of Polarisation Splitting in planar Microcavities.	51
4.1	The Sample.	51

4.2	The Measurement.	54
4.3	Results.	54
5	Experimental Proof of spatial Mode Locking in planar Microcavities.	60
5.1	The Sample.	60
5.2	The Measurement.	63
5.3	Results.	65
6	Conclusion and Outlook.	78
6.1	Conclusion.	78
6.2	Outlook.	79
	Appendix.	81
	Publications.	81
	List of Symbols.	81
	Bibliography.	83
	Acknowledgements.	86

1 Introduction.

Overview.

In this work, studies on the cavity modes of planar microcavities are presented. The term *planar* denotes that the cavities are homogeneous along the cavity plane, i.e. unstructured. The investigated cavities contain an optically active organic material, bound by distributed Bragg reflectors (DBRs) as the cavity mirrors.

This work consists of two parts: In the first part, studies on the polarisation properties of the cold cavity modes are presented. *Cold* means that the organic material is excited so weakly, that the excitation does not change the optical properties of the microcavity. It is shown that, in general, in a cavity with DBR mirrors, the cavity mode splits into two modes which are orthogonally polarised. The dependence of this mode splitting on angle and on cavity thickness is theoretically and experimentally studied.

The spatial shape of the cavity mode, mainly the distribution of the electromagnetic field in the cavity plane, is an important issue when constructing a laser with these microcavities. Lasing will only take place if the overall losses are compensated by gain. Wherever the electric field of the cavity modes penetrates, it is subjected to the absorption of the cavity material. Further losses occur due to the mirrors (absorption, and transmission to the outside). All these effects must be compensated by gain to obtain lasing. The excitation threshold for lasing is reached when the gain, weighted with the electric amplitude of the photon field and integrated over the cavity, exceeds the overall losses. The spatial distribution of gain and loss therefore influences how high in the excited regions the material gain per volume, and so the pumping intensity, has to be in order to achieve lasing.

The second part thus deals with the size of cold cavity modes; investigated is the spatial extension of the modes along the cavity plane. Furthermore, the growth of the cavity modes is discussed for non-cold cavities. Under excitation above the laser threshold, cavity

modes which overlap may lock their individual phases. Experiments showing this phase locking of spatial cavity modes are presented. These hopefully help to understand which spatial shape of optical pumping is optimal in order to achieve lasing.

The structure of this work is as follows:

Chapter 2 presents the theoretical framework. Therein, basic notions for the description of electromagnetic waves are given (section 2.1). Processes of light emission and the laser principle is explained (section 2.2). The Fresnel formulae and the transfer matrix method are presented (sections 2.3 and 2.4). Sections 2.5 and 2.6 introduce DBR mirrors and microcavities and their optical properties. Polarisation splitting of the cavity modes is discussed. An analytical approximation, which enables one to calculate the angle and spectrally dependent transmission behaviour of a DBR microcavity, is given, including absorption and gain of the cavity medium (sections 2.7 and 2.8). Compared to section 2.6, where only the angle dependent resonance frequency is of interest, here, the transmission for a whole spectral range is discussed, making statements about the width of the cavity mode possible. The notion of the in plane size of cavity modes is laid out, and the effect of gain on the mode radius is discussed shortly (section 2.9). Phase locking of spatial cavity modes above lasing threshold is introduced (section 2.10).

In chapter 3, the experimental setup used for the measurements is described.

Chapter 4 presents the experimental studies on polarisation splitting of the cavity modes: The sample and the measurement method are described (sections 4.1 and 4.2), and the results are discussed (section 4.3). Corresponding calculations are presented and compared with the measurements (section 4.3).

Experiments on spatial mode locking are reported in chapter 5: After describing the sample and the measurement (sections 5.1 and 5.2), the results are presented and discussed (section 5.3).

Finally, a conclusion and an outlook are given (chapter 6).

Author's contribution.

The content of the whole chapter 2, namely the theoretical considerations, is taken from literature—directly or with modifications with ideas from other external sources. Only the numerical transfer matrix calculations to produce figures illustrating aspects of the theory were performed by the author of this work.

Most of the measurement setup, explained in chapter 3, including the modification mentioned in section 5.2, was already built by other members of the research group in the past. The author of this work did only do minor modifications to the preexisting setup to get the setup mentioned in the text.

The chapters 4 and 5 describe tasks conducted by the author of this work, except the sample preparation (sections 4.1 and 5.1), which was done by other members of the research group.

Conventions.

Throughout this work, the following convention for a coordinate system will be used:

When not mentioned otherwise, the coordinate system used will be defined to be Cartesian. The z axis will be parallel to the normal direction of the sample or the cavity or the distributed Bragg reflector, whereas the x and y axes will lie parallel to the sample / cavity / mirror plane (refer to figure 3.1 on page 47 for this definition of the coordinate system).

2 Theoretical Basis.

2.1 Ways of describing Light.

This section introduces basic ways of describing light, and the notation used in this work for describing plane harmonic electromagnetic waves.

Light can be described in several ways:

1. As an electromagnetic wave, characterised by its frequency and direction of propagation and determined by the physical laws dictated by Maxwell's equations.
2. As a collection of the elementary particles which are called *photons*. Each photon has an energy which corresponds to the frequency in the electromagnetic wave picture and propagates in a specific direction.
3. If the spatial scale of description is much larger than the wavelength, the propagation can be described in terms of rays.

In this work, the wave description will mostly be used.

An arbitrary electromagnetic wave can be decomposed into an integral over so called plane waves. Plane waves are harmonic waves with one definite frequency which propagate in one definite direction and extend infinitely in space. In the following, the notations used for these waves are laid out.

Let the electric field vector \vec{E} of a general electromagnetic harmonic plane wave be given as

$$\vec{E} = \Re \left[\vec{E}_0 \cdot e^{i(\omega t - \vec{k}\vec{r}) + i\phi} \right] = \Re \left[\vec{E}_0 \cdot e^{i\omega \left(t - \frac{n}{c} \vec{s}\vec{r} \right) + i\phi} \right], \quad (2.1)$$

where \vec{E}_0 is the electric field amplitude of the wave, ω the angular frequency, \vec{k} the wave vector, and ϕ a constant phase of the electromagnetic wave, $\vec{s} = \frac{\vec{k}}{|\vec{k}|}$ the unit vector in

propagation direction, n the refractive index of the medium the wave is propagating in, c the speed of light in vacuum, \vec{r} and t are the location and time for which to evaluate \vec{E} and \Re denotes the mapping returning the real part of its argument. A complex amplitude \vec{A} of the electric part of the electromagnetic field is defined as

$$\vec{A} = \vec{E}_0 \cdot e^{i\phi}; \quad (2.2)$$

it incorporates the amplitude and vectorial polarisation (\vec{E}_0) as well as the phase ($e^{i\phi}$) of the electric wave. The frequency and propagation direction (ω and \vec{s}) and the temporal and spatial dependence are kept out of \vec{A} . With equation (2.2), the electric field wave (2.1) becomes

$$\vec{E} = \Re \left[\vec{A} \cdot e^{i(\omega t - \vec{k}\vec{r})} \right] = \Re \left[\vec{A} \cdot e^{i\omega \left(t - \frac{n}{c} \vec{s}\vec{r} \right)} \right]. \quad (2.3)$$

Later, sometimes only the length $|\vec{A}| =: A$ of the complex electric amplitude will be used, but it will also be called complex electric amplitude. It will be clear that the vectorial character is not important.

Note, that for describing an electromagnetic wave, it is sufficient to describe the electric part, because the equation [2]

$$\vec{B} = \frac{1}{c} \vec{s} \times \vec{E} \quad (2.4)$$

relates the magnetic field \vec{B} to the electric field.

2.2 Stimulated Emission and Lasing.

Originally, the term laser is an abbreviation for light amplification by stimulated emission of radiation. Nowadays it is not only used as an abbreviation. Rather, laser is also used as a term for devices which emit light by the laser principle (“(a) laser”), and for the light which is produced by a laser (“laser light”). Also as a verb the word is used, describing the act of emitting laser radiation (“(to) lase”).

The laser principle is explained in this section. Most of the details presented here are adopted from the diploma thesis of Schütte [3].

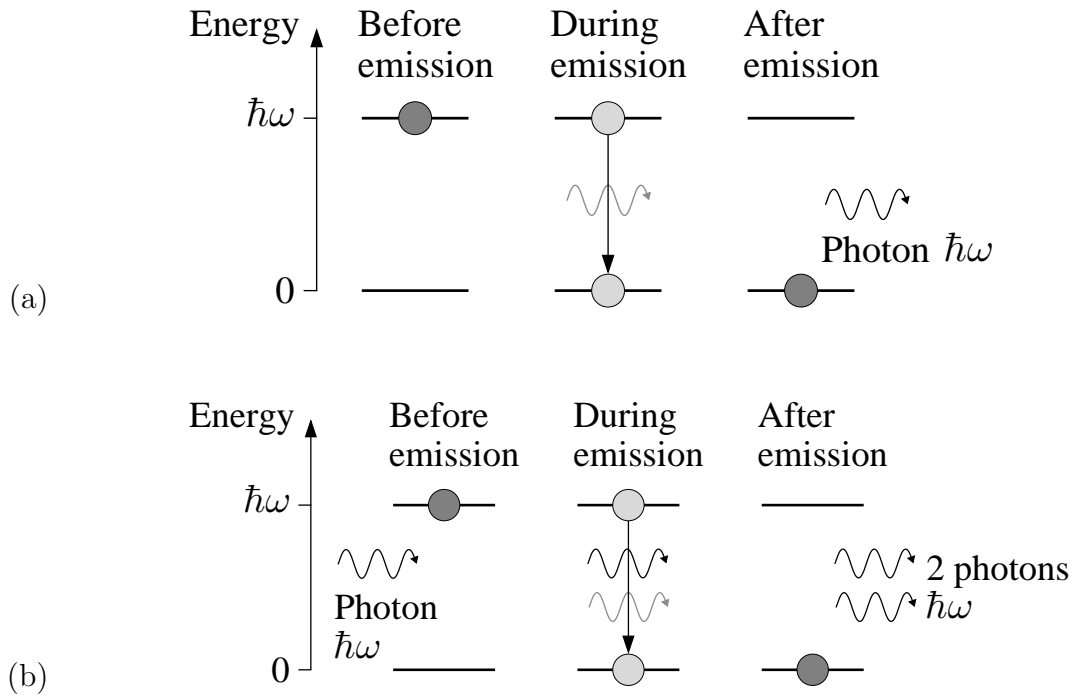


Figure 2.1: Spontaneous (a) and stimulated (b) emission in a two level system. The energy difference between the excited state and the ground state is $\hbar\omega$. The emission in (a) occurs statistically with a characteristic time τ . The emission in (b) occurs exactly when the incoming photon passes the system.

2.2.1 Photon Emission Processes.

For simplicity consider an optically active system with only two energetic levels. This is a model system for an atom with an electron that can be excited, or an excitable molecule. If the system is energetically excited, it can relax and emit the stored energy as light in the form of one photon. The photon then carries the excitation energy. This emission process can occur in two ways:

1. As *spontaneous emission*. Spontaneous emission is characterised by a time τ . τ is the *life time* of the excited state. It is statistically defined for an ensemble of excited systems: τ is the time after which the $\frac{1}{e}$ th fraction of the originally excited systems are still excited; the others did already decay and emit a photon. Spontaneous emission is a statistical process, and each excited two level system emits independently from all the others.

2. As *stimulated emission*. Stimulated emission can occur when an excited system is traversed by a photon with an energy of the same value as the energy of the excited state. The excited state can then decay and emit a second photon which has the same energy, momentum and polarisation as the first, initiating, photon. Because both photons have the same properties, they are *coherent* with respect to each other.

Also, the reverse process can happen: If the system is not excited, a photon with matching energy can be absorbed and excite the system.

Figure 2.1 shows schematically the process of spontaneous and stimulated emission. The energy $\hbar\omega$ of the emitted photon coincides with the energy difference $\hbar\omega_0$ between the excited state and the ground state. However, the photon energy does not exactly equal that energy. Rather, it is distributed around the energy value of the excited state with a width $\Delta\hbar\omega = \frac{\hbar}{2\tau}$ given by Heisenberg's uncertainty principle.

Most systems are not simple two level systems as the one described here, but the basic principles remain the same nonetheless.

2.2.2 Light Amplification, Gain and Laser Threshold.

Because the photon emitted by stimulated emission has the same properties as the photon which induced the emission, light can be amplified using this effect. An optically active medium contains many atoms or molecules which can emit or absorb light. The macroscopic ability of such a medium to amplify light by stimulated emission is called *gain*. When a medium is *cold*, all its emitters are in the ground state. By external excitation of the material, for example using light with a matching photon energyⁱ, some of the atoms or molecules will be excited. This process is called *pumping*. The excited emitters can relax by spontaneous or stimulated emissionⁱⁱ.

If the radius of the optically active material is small compared to the average pathlength which photons travel before they are re-absorbed by the material or before they can stimulate an emission, then almost all emitted photons leave the medium without any further interaction. In this case, almost all the internal emission comes from spontaneous emission (if there is no intense external source which triggers stimulated emission). On

ⁱSome systems can also be excited electronically, for example.

ⁱⁱThere are also other—non-radiative—forms of relaxation. They are not discussed here.

the other hand, if the extension of the optically active material is large compared to the mean free path of a photon travelling inside it, the following two things are possible:

1. If the overall absorption of photons—due to excitation of molecules or atoms, but also due to other, dissipative, effects—is higher than the gain, spontaneous emission is the main type of emission in the system. This regime is called the regime of spontaneous emission.
2. If the gain compensates (or overcompensates) all absorption, each emitted photon stimulates the emission of one (or more) further photons, on average. This regime is called the laser regime. The generated radiation is dominated by stimulated emission, and the emitted light is coherent.

When the device is operating in the regime of spontaneous emission, light is emitted into all possible modesⁱⁱⁱ, whereas in the laser regime most of the emission takes place into the laser mode. The so called β factor is defined as the ratio between the spontaneous emission power $P_{\text{laser}}^{\text{spontaneous}}$ coupled into the actual laser mode and the total power $P_{\text{total}}^{\text{spontaneous}}$ of radiation emitted by spontaneous emission:

$$\beta = \frac{P_{\text{laser}}^{\text{spontaneous}}}{P_{\text{total}}^{\text{spontaneous}}}. \quad (2.5)$$

β is defined by the properties of the material in the regime of spontaneous emission. A *generalised β factor* β' will be introduced: It is the emission power P_{laser} released into the laser mode over the total emission power P_{total} , regardless whether the sample is in the regime of spontaneous or stimulated emission:

$$\beta' = \frac{P_{\text{laser}}}{P_{\text{total}}}. \quad (2.6)$$

When the device is in the laser regime, where stimulated emission dominates, most of the excited states quickly get deexcited by stimulated emission, thus all emitting into the same mode. That is why β' is almost 1 in the laser regime, while in general it is smaller by orders of magnitude in the regime of spontaneous emission.

ⁱⁱⁱPossible modes are on the one hand determined by the geometry of the surrounding, e.g. whether the emitter is placed inside a cavity, and on the other hand by the spectral width of the emitter. Note that also a theoretical emitter with vanishing spectral width can emit into infinitely many modes, because each direction of emission corresponds to a different mode.

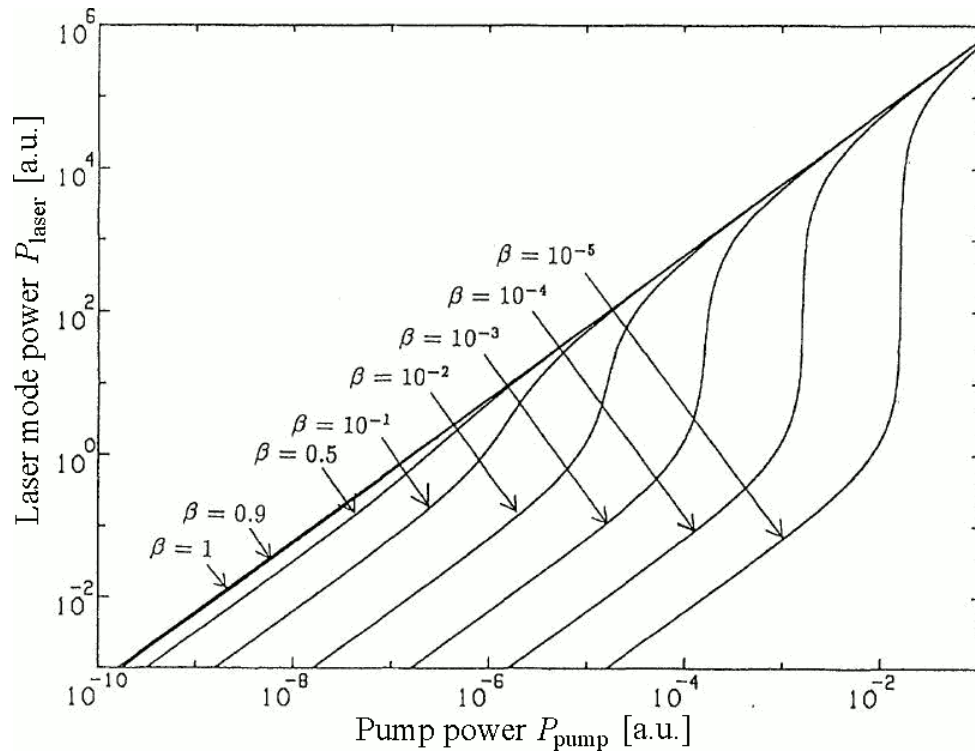


Figure 2.2: Theoretical input output curves for a laser. Shown are curves for different values of the β factor. The figure is taken from [3] and has been slightly modified.

The curve relating the output power P_{laser} (or intensity) of the laser mode to the power P_{pump} (or intensity) of the external pumping is called *input-output-curve* of a laser. With increasing P_{pump} , P_{laser} increases linearly in the spontaneous emission regime. Also the gain increases with the pumping power. At a level where the gain just compensates all losses, lasing starts, and P_{laser} increases rapidly by $\frac{1}{\beta}$. This very small region of P_{pump} where P_{laser} almost jumps is called the *laser transition*, and the value of P_{pump} where it takes place is the *laser threshold*. After the laser transition, P_{laser} increases linearly again with P_{pump} . Figure 2.2 shows theoretical input output curves for different values of β . It can be seen that the higher β , the lower the laser threshold. Note that for lasers with β close to 1 the laser transition is not discernible in the input-output-curves, that is why this case is often referred to as the *thresholdless laser*.

2.2.3 Emission in optical Resonators and Purcell Effect.

An optical resonator consists in the simplest case of just two plane mirrors, which are parallel and enclose some space. Cavities as described in section 2.6 are optical resonators. If some emitting material is placed inside a resonator, emitted light may traverse the medium several times before it escapes the mirrors. Light is reflected multiple times through the active medium, which increases the probability of the photons to interact with the medium. That is why in this case a small amount of active material can be enough to achieve lasing, even if the extension of the material is smaller than the mean free path of a laser mode photon.

Within a resonator, also another effect occurs: The *Purcell effect*. Purcell [4] did describe the modification of the spontaneous emission lifetime τ for individual modes when the excitable system is put inside a cavity: Cavity quantum electrodynamics determines the spontaneous emission by the interaction between the optically active medium and the vacuum radiation modes. If the vacuum states are altered, also the spontaneous emission lifetime changes. If the emitter is placed in a cavity, the rate of emission into the discrete cavity modes is increased, whereas for modes forbidden by the cavity the emission is decreased. If the laser mode is a cavity mode, the Purcell effect increases β . Therefore, with a good cavity, the laser threshold can be decreased notably compared to its level without a cavity.

2.3 Review of the Fresnel Formulae.

The so-called Fresnel formulae describe the amplitude and phase of reflected and transmitted light impinging on a medium boundary, separately for TE and TM polarised light. In this section, a short review of the Fresnel formulae is given, following the book [2] by Born and Wolf.

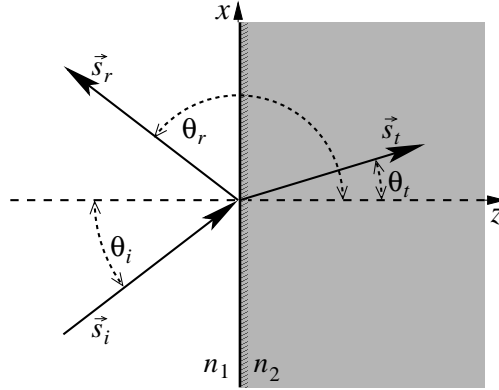


Figure 2.3: Refraction and reflection of a plane wave impinging on a medium boundary.

Consider a plane boundary between two media. Let the media be called medium 1 and medium 2, with respective refractive indices n_1 and n_2 . Now, let the wave described by equation (2.3) originate from somewhere inside medium 1 and impinge on that boundary. Let the coordinate system be defined such that the medium boundary lies in the x - y -plane and the light is propagating in the x - z -plane (the so called *plane of incidence*). The situation is depicted in figure 2.3. The incident wave is marked with \vec{s}_i and encloses an angle θ_i with the z -axis, the reflected wave is marked with \vec{s}_r and encloses an angle θ_r with the z -axis, and the transmitted wave is labelled \vec{s}_t and forms an angle θ_t with the z -axis.

Due to the choice of the coordinate system, \vec{k} is perpendicular to the y -direction. Thus, equation (2.3) can be written as

$$\vec{E} = \Re \left[\vec{A} \cdot e^{i\omega \left(t - \frac{n}{c} (x \sin \theta_i - z \cos \theta_i) \right)} \right]. \quad (2.7)$$

This field can be decomposed into two vectorial components which are orthogonal with respect to each other and have their own value of ϕ each. These components are called *polarisations* of the light.

Let one of the components be parallel to the plane of incidence. This component will be indexed by \parallel and called *transverse magnetic* (TM-) or *p*-polarisation. The other component is defined to be perpendicular to the incidence plane and will be indexed by \perp and called *transverse electric* (TE-) or *s*-polarisation.

Let A_i denote the complex electric amplitude of the incident wave, A_t the complex electric amplitude of the transmitted and A_r the complex electric amplitude of the reflected wave. For media which have zero conductivity and a relative magnetic permeability μ_r equal to one, the book [2] gives the Fresnel formulae, relating $A_{t\parallel}$, $A_{t\perp}$, $A_{r\parallel}$ and $A_{r\perp}$ to $A_{i\parallel}$, $A_{i\perp}$, θ_i and θ_t , as follows:

$$\begin{aligned} A_{t\parallel} &= \frac{2 \cos \theta_i \sin \theta_t}{\sin (\theta_i + \theta_t) \cos (\theta_i - \theta_t)} \cdot A_{i\parallel}, \\ A_{t\perp} &= \frac{2 \cos \theta_i \sin \theta_t}{\sin (\theta_i + \theta_t)} \cdot A_{i\perp}, \\ A_{r\parallel} &= \frac{\tan (\theta_i - \theta_t)}{\tan (\theta_i + \theta_t)} \cdot A_{i\parallel}, \\ A_{r\perp} &= -\frac{\sin (\theta_i - \theta_t)}{\sin (\theta_i + \theta_t)} \cdot A_{i\perp}. \end{aligned} \tag{2.8}$$

Using the *law of refraction*, $n_1 \sin \theta_i = n_2 \sin \theta_t$, θ_i or θ_t can be eliminated if one wishes, thereby including n_1 and n_2 into the formulae. The angles in the above equations are bounded by 0 and $\frac{\pi}{2}$ (the case of total internal reflection is not considered here).

Under some conditions, A_r obtains a phase shift of π upon reflection, which corresponds to a multiplication of A by $-1 = e^{i\pi}$. The phase shift will be determined by looking at the signs of the expressions for the reflected amplitudes in the equations (2.8) and utilising $n_2 \gtrless n_1 \Leftrightarrow \theta_t \gtrless \theta_i$: $A_{r\perp}$ is phase shifted by π with respect to $A_{i\perp}$ in the case of $n_2 > n_1$. $A_{r\parallel}$ is phase shifted by π with respect to $A_{i\parallel}$ if

1. $n_2 > n_1$ and $\theta_i + \theta_t > \frac{\pi}{2}$ or
2. $n_2 < n_1$ and $\theta_i + \theta_t < \frac{\pi}{2}$.

In all other cases, the phase shift is 0 or there is no light reflected.

The *amplitude transmission coefficient* t for the transmitted amplitude is defined as the ratio of the transmitted amplitude with the incident amplitude: $t := \frac{A_t}{A_i}$. Similarly, the

reflection coefficient r is defined as $r := \frac{A_r}{A_i}$. From equation (2.8), t and r follow to be

$$\begin{aligned} t_{\parallel} &= \frac{2 \cos \theta_i \sin \theta_t}{\sin (\theta_i + \theta_t) \cos (\theta_i - \theta_t)}, \\ t_{\perp} &= \frac{2 \cos \theta_i \sin \theta_t}{\sin (\theta_i + \theta_t)}, \\ r_{\parallel} &= \frac{\tan (\theta_i - \theta_t)}{\tan (\theta_i + \theta_t)} \text{ and} \\ r_{\perp} &= -\frac{\sin (\theta_i - \theta_t)}{\sin (\theta_i + \theta_t)}. \end{aligned} \quad (2.9)$$

What happens if the light path is reversed in such a way that the incident light is now coming from the path of the transmitted light in the previous discussion? The following nomenclature is being used: Quantities with a tilde (\sim) on top will belong to the new case where light is going the reverse direction, quantities without a tilde belong to the original case. Thus, it is

$$\begin{aligned} \tilde{\theta}_i &= \theta_t, \\ \tilde{\theta}_t &= \theta_i, \\ \tilde{n}_1 &= n_2 \text{ and} \\ \tilde{n}_2 &= n_1. \end{aligned} \quad (2.10)$$

From equations (2.9) it follows

$$\begin{aligned} \tilde{t}_{\parallel} &= \frac{2 \cos \theta_t \sin \theta_i}{\sin (\theta_i + \theta_t) \cos (\theta_t - \theta_i)}, \\ \tilde{t}_{\perp} &= \frac{2 \cos \theta_t \sin \theta_i}{\sin (\theta_i + \theta_t)}, \\ \tilde{r}_{\parallel} &= \frac{\tan (\theta_t - \theta_i)}{\tan (\theta_i + \theta_t)} \text{ and} \\ \tilde{r}_{\perp} &= -\frac{\sin (\theta_t - \theta_i)}{\sin (\theta_i + \theta_t)}. \end{aligned} \quad (2.11)$$

With the relations $\sin(-x) = -\sin(x)$, $\cos(-x) = \cos(x)$, $\tan(-x) = -\tan(x)$, $n_1 \sin \theta_i = n_2 \sin \theta_t$ (law of refraction) and $\cos(\arcsin x) = \sqrt{1 - x^2}$ it follows for both, TE and TM, polarisations:

$$\begin{aligned}\tilde{t} &= t \cdot \frac{\tan \theta_i}{\tan \theta_t} = t \cdot \frac{\sqrt{\left(\frac{n_2}{n_1}\right)^2 - \sin^2 \theta_i}}{\cos \theta_i} \text{ and} \\ \tilde{r} &= -r.\end{aligned}\tag{2.12}$$

Also, the following relation holds true:

$$t\tilde{t} - r\tilde{r} = 1.\tag{2.13}$$

2.4 Review of Transfer Matrix Calculations.

In this section, a principal derivation of the transfer matrix method will be given, which is being used to calculate optical properties of unstructured (planar) microcavities. This derivation is inspired by and roughly follows the lecture notes of Sernelius [5].

Consider a stack of N vertical plane parallel layers of dielectric materials, illuminated from the left with monochromatic, parallel light. The electromagnetic wave travelling within this stack can, at each point, be described as a superposition of a left and a right propagating plane wave. Firstly, the influence of an arbitrary single layer on the electric field propagating through it is studied. Secondly, the N layers are put together so that the transmission and reflection of the whole stack can be calculated.

Investigating a single layer, the notations and definitions as given in figure 2.4 and its caption are used. By R , the complex electric amplitude of the right propagating wave is referred to, similarly, L denotes the complex electric amplitude of the left travelling wave.

The amplitudes of the incoming waves with respect to layer i are referred to by R_i and L_{i+1} , of the outgoing ones by L_i and R_{i+1} . So, L_i and R_{i+1} both depend only on R_i and L_{i+1} as well as on the properties of the layers $i - 1$, i and $i + 1$. The layer properties are expressed in terms of the transmission and reflection coefficients of, as well as the phase delays due to travel through the layers. The outgoing waves can therefore be characterised

by

$$\begin{aligned} R_{i+1} &= t_{i-1,i} e^{i\delta_i} R_i + e^{i\delta_i} r_{i,i-1} e^{i\delta_i} L_{i+1} \text{ and} \\ L_i &= r_{i-1,i} R_i + e^{i\delta_i} t_{i,i-1} L_{i+1}, \end{aligned} \quad (2.14)$$

where $t_{a,b}$ resp. $r_{a,b}$ is the transmission resp. reflection coefficient for light which comes from layer a and impinges on the boundary to layer b , and δ_a is the phase shift the light obtains while travelling through layer a once. δ_a can be expressed as

$$\delta_a = \frac{\ell_a}{\cos \theta_a} \frac{\omega n_a}{c} \quad (2.15)$$

(refer to equation (2.1)), where ℓ_a is the thickness of layer a , θ_a the angle, with respect to the layer boundary normal, of propagation inside layer a and n_a the refractive index of layer a . With some algebraic transformation, R_i and L_i can be expressed in terms of R_{i+1}

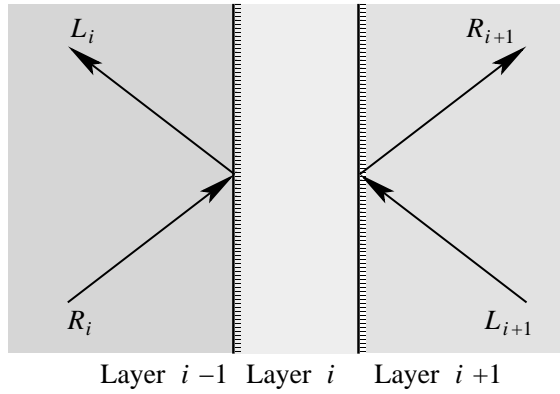


Figure 2.4: The definition of the elements used for the derivation of the transfer matrix method. The left interface of layer i is defined as completely belonging to layer i . So, R_i denotes the complex amplitude of the wave travelling to the right, evaluated at the right edge of layer $i-1$, just before entering layer i . Similarly, L_i denotes the complex amplitude of the wave travelling to the left, evaluated at the right edge of layer $i-1$, just after leaving layer i . The indexing of the layers increases to the right.

and L_{i+1} , which can be written in matrix notation:

$$\begin{pmatrix} R_i \\ L_i \end{pmatrix} = \frac{1}{t_{i-1,i}} \begin{pmatrix} e^{-i\delta_i} & r_{i-1,i}e^{i\delta_i} \\ r_{i-1,i}e^{-i\delta_i} & e^{i\delta_i} \end{pmatrix} \begin{pmatrix} R_{i+1} \\ L_{i+1} \end{pmatrix} =: \mathbf{M}_i \begin{pmatrix} R_{i+1} \\ L_{i+1} \end{pmatrix}, \quad (2.16)$$

where the relations (2.12), relating $r_{i-1,i}$ and $r_{i,i-1}$, and (2.13) were used. The matrix

$$\mathbf{M}_i = \frac{1}{t_{i-1,i}} \begin{pmatrix} e^{-i\delta_i} & r_{i-1,i}e^{i\delta_i} \\ r_{i-1,i}e^{-i\delta_i} & e^{i\delta_i} \end{pmatrix} \quad (2.17)$$

is called the *transfer matrix* for layer i .

With equation (2.16), the fields directly left of layer i are related to the fields at the right edge of layer i ; i is arbitrary. More general, for an arbitrary j ($j \leq i$), the fields left of layer j can be related to the fields just at the right edge of layer i in the following way: The transfer matrices of the layers $j, j+1, \dots, i$ are put one after another, $\mathbf{M}_1\mathbf{M}_2 \cdots \mathbf{M}_N$. The transfer matrix \mathbf{M} of the whole layer stack, including the rightmost surface, can thus be obtained by

$$\mathbf{M} = \mathbf{M}_1\mathbf{M}_2 \cdots \mathbf{M}_N\mathbf{M}_{\text{rs}_N}, \quad (2.18)$$

where the matrix \mathbf{M}_{rs_N} describes the transfer through and reflection at the right surface of the rightmost layer. It has to be included since in the derivation the surface left of a layer was assumed to belong to that layer, and thus the rightmost surface of the stack, where there is no more layer coming, has to be included by hand. This matrix is given by

$$\mathbf{M}_{\text{rs}_N} = \frac{1}{t_{N,N+1}} \begin{pmatrix} 1 & r_{N,N+1} \\ r_{N,N+1} & 1 \end{pmatrix}. \quad (2.19)$$

Indices equal to 0 and $N+1$ refer to the medium directly left of and right of the layer stack, respectively. \mathbf{M} is relating the fields just left of the whole stack to the fields just right of it. Denoting by R'_N resp. L'_N the right travelling resp. left travelling fields just outside the stack on its right side (thus, just behind the right side of the right border of layer N), the following holds true:

$$\begin{pmatrix} R_0 \\ L_0 \end{pmatrix} = \mathbf{M} \begin{pmatrix} R'_{N+1} \\ L'_{N+1} \end{pmatrix} =: \begin{pmatrix} M_{11} & M_{12} \\ M_{21} & M_{22} \end{pmatrix} \begin{pmatrix} R'_N \\ L'_N \end{pmatrix}, \quad (2.20)$$

where M_{ij} is the ij -component of \mathbf{M} .

To obtain the reflection and transmission coefficients r and t of the whole stack, it is assumed that only from one side light is shining onto the system. The reflected and transmitted amplitudes of that light are calculated. This is done for two cases, firstly, the light comes from the left side, secondly, it comes from the right side. This yields r and t for both directions.

In the first case to deal with, light is shining only from the left side onto the stack. Thus the complex amplitudes to consider are A_i for the incident light (from the left), A_r for the reflected light (to the left) and A_t for the transmitted light (to the right) (following the previous nomenclature, $A_i = R_0$, $A_r = L_0$, $A_t = R'_N$, and $L'_N = 0$). So, on the one hand it is

$$\begin{aligned} A_r &= r_R A_i \text{ and} \\ A_t &= t_R A_i, \end{aligned} \tag{2.21}$$

where the index R means that these are the reflection and transmission coefficients for incident light coming from the left propagating to the right, and on the other hand

$$\begin{pmatrix} A_i \\ A_r \end{pmatrix} = \begin{pmatrix} M_{11} & M_{12} \\ M_{21} & M_{22} \end{pmatrix} \begin{pmatrix} A_t \\ 0 \end{pmatrix}. \tag{2.22}$$

Comparing equations (2.21) and (2.22), one finds

$$\begin{aligned} r_R &= \frac{M_{21}}{M_{11}}, \\ t_R &= \frac{1}{M_{11}}. \end{aligned} \tag{2.23}$$

The same argument can be done for the second case where light shines from the right side only onto the stack. Via

$$\begin{pmatrix} 0 \\ A_t \end{pmatrix} = \begin{pmatrix} M_{11} & M_{12} \\ M_{21} & M_{22} \end{pmatrix} \begin{pmatrix} A_r \\ A_i \end{pmatrix}, \tag{2.24}$$

this leads to

$$r_L = -\frac{M_{12}}{M_{11}} \text{ and}$$

$$t_L = \frac{M_{12}M_{21}}{M_{11}} + M_{22}. \quad (2.25)$$

Here, the index L means that the coefficients are for incident light coming from the right, propagating to the left.

With the method described above, the reflection and transmission coefficients of a stack of plane parallel layers can be calculated according to equations (2.23) and (2.25). For this, the transfer matrix \mathbf{M} of the stack has to be constructed from the properties of the individual layers.

2.5 Dielectric Bragg Reflectors (DBRs).

Distributed Bragg reflectors, *short DBRs or dielectric mirrors, are mirrors which have very high reflection coefficients (typically in the order of 99.9%) within a given spectral region and are fairly transparent within other spectral regions. Here, DBRs and their basic properties will be introduced.*

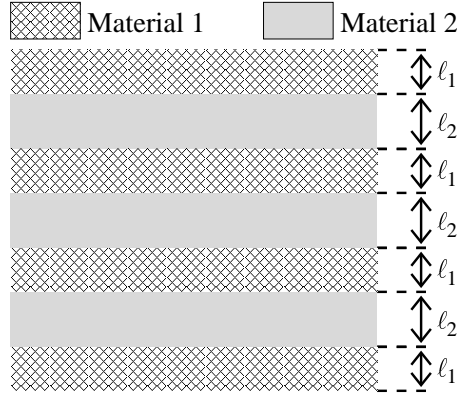


Figure 2.5: Cross sectional sketch of a DBR.

A DBR is a mirror of the following kind: An alternating stack of layers of two, ideally non-absorbing, materials (see figure 2.5), where the refractive indices of both materials

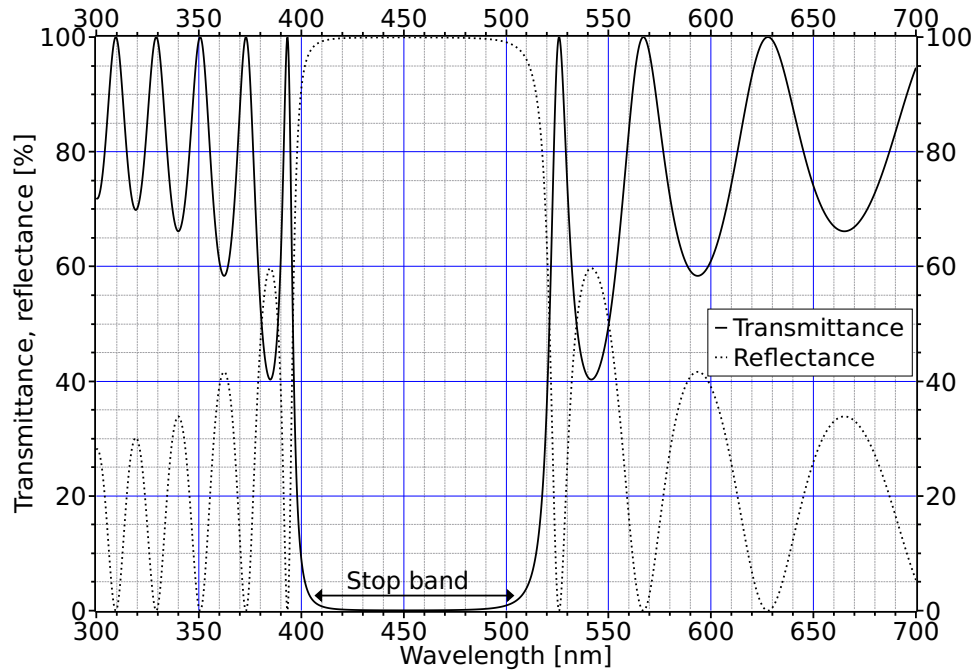


Figure 2.6: Typical transmission and reflection spectrum of a DBR. The design comprises TiO_2 as material 1 ($n_1 = 2.19$) and SiO_2 as material 2 ($n_2 = 1.45$) with an optical layer thickness of 112.5 nm, leading to a the stop band centred around 450 nm. The spectrum is calculated using a software (SCI FilmWizard, [6]) which utilises the transfer matrix method.

differ.

Ideally, the optical thickness^{iv} of each layer is the same. Only this case will be dealt with here. One material will be called material 1, the other material 2. Consequently, the refractive index of material i will be called n_i and the thickness of a layer made of material i ℓ_i .

The optical thickness $n_i \ell_i$ of each layer being the same implies

$$n_1 \ell_1 = n_2 \ell_2. \quad (2.26)$$

The transmission and reflection spectra of such a DBR can be calculated with the transfer matrix method described in section 2.4, where the wavelength (or angular frequency) of the light is incorporated by equation (2.15). Figure (2.6) shows the calculated spectra

^{iv}The optical thickness of a layer is its (physical) thickness multiplied by its refractive index.

of transmitted and reflected intensity for a DBR with the following design: $n_1 = 2.19$, $n_2 = 1.45$, 11 layers of material 1, 10 layers of material 2 (between material 1 layers), $n_i \ell_i = 112.5 \text{ nm}$. Such a DBR shows very high reflectance ($\sim 99.9\%$) within a wavelength range, called the *stop band*. The stop band is centred around a wavelength called λ_s , the wavelength of the *centre of the stop band*. λ_s is given by the Bragg condition of constructive interference of all the light beams reflected at all layer boundaries. With λ_s known, the angular frequency of the centre of the stop band is

$$\omega_s = \frac{2\pi c}{\lambda_s}. \quad (2.27)$$

For propagation angles parallel to the DBR normal direction,

$$\omega_s = \frac{m\pi c}{2n_i \ell_i}, \quad (2.28)$$

with $m \in \mathbb{N} \setminus \{0\}$. Relation (2.28) directly follows from the Bragg condition. For oblique propagation, Panzarini et al. [7, 8] give appropriate expressions, different for TE and TM polarisation. For $n_1 > n_2$, they are for the lowest order ($m = 1$) stop band:

$$\begin{aligned} \omega_s^{\text{TE}} &= \frac{\pi c (n_1 \cos \theta_1 + n_2 \cos \theta_2)}{2n_1 n_2 (\ell_1 + \ell_2) \cos \theta_1 \cos \theta_2} \text{ and} \\ \omega_s^{\text{TM}} &= \frac{\pi c (n_1 \cos \theta_2 + n_2 \cos \theta_1)}{2n_1 n_2 (\ell_1 \cos^2 \theta_1 + \ell_2 \cos^2 \theta_2)}, \end{aligned} \quad (2.29)$$

where θ_i is the propagation angle inside material i . In the example of figure (2.6), the incidence of the light is in the normal direction ($\theta = 0^\circ$), and λ_s is 450 nm. The transmitted intensity is one minus the reflected intensity, because absorption is neglected.

2.6 DBR Microcavities and Polarisation Properties.

2.6.1 Introduction to DBR microcavities.

When two plane parallel mirrors enclose a small gap, an optical cavity is formed. In this section, cavities with DBR mirrors, their basic properties, polarisation properties and electromagnetic field enhancement effects are presented.

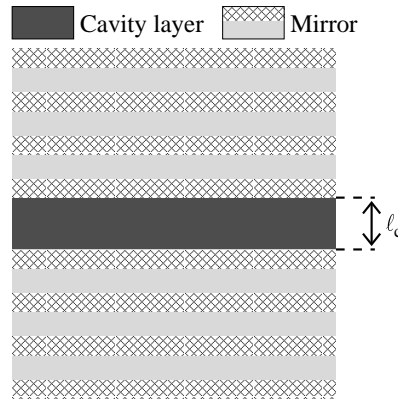


Figure 2.7: Vertical cross sectional drawing of a DBR microcavity.

It is possible to create an optical cavity by sandwiching a layer of an optically transparent material between two DBRs. If the thickness of this *cavity layer* is in the order of micrometers, the device is called a *microcavity* or, in the special case with dielectric mirrors, *DBR microcavity*. Figure 2.7 shows a cross sectional sketch of a DBR microcavity. The thickness of the cavity layer is denoted by ℓ_c .

Due to the cavity layer, the transmission spectrum of the device differs qualitatively from that of a pure DBR: For each wavelength within the stop band, that fulfils the resonance condition of the cavity, the DBR microcavity has a high and spectrally narrow transmission peak (and, consequently, shows low reflectance at this spectral position). Each spectral region, for which this cavity resonance condition is met, is called *cavity mode*. Cavity mode wavelengths are denoted by λ_m , and, conversely, cavity mode angular frequencies by ω_m . Figure 2.8 shows a transmission spectrum of a DBR microcavity which is made of a cavity layer with refractive index $n_c = 1.7$ and thickness $\ell_c = 443.38 \text{ nm} = 3.94 \frac{\lambda_s}{4}$, surrounded by two DBR mirrors of the same type as used for making the spectra in figure 2.6. The spectrum is calculated using the software FilmWizard [6] from Scientific Computing International. The spectrum shows two cavity modes, one at 408.99 nm, the other at 477.45 nm. In this example, the light propagates parallel to the cavity normal direction ($\theta = 0^\circ$).

Before dealing with the theory of DBR microcavities, a short look will be taken on “classical” cavities. These are cavities bound by two “normal”, surface reflecting mirrors. These mirrors induce a phase shift of exactly 0 or π to reflected light (but nothing in

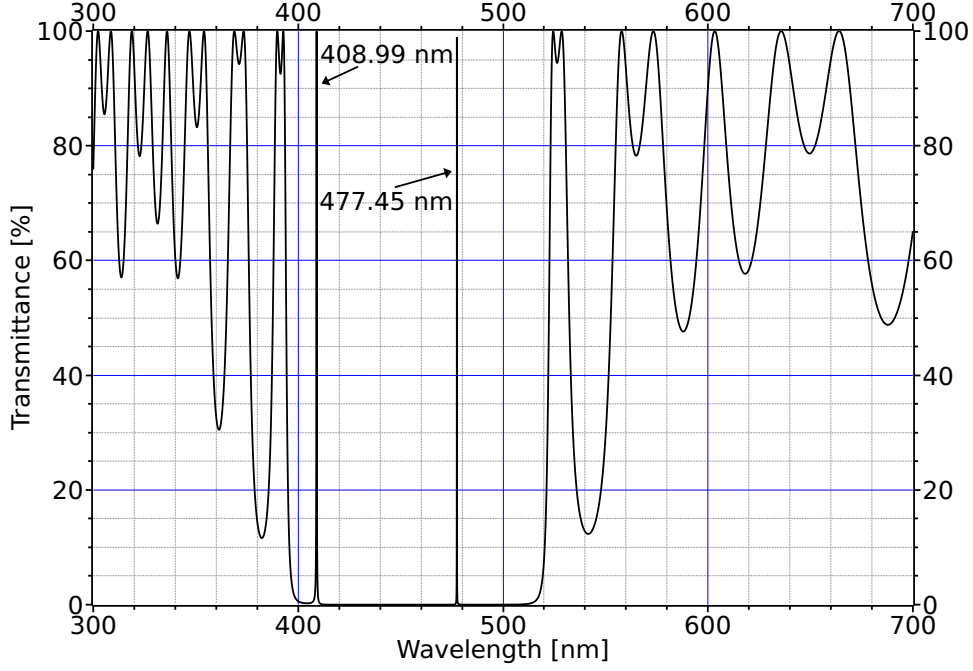


Figure 2.8: Calculated transmission spectrum of a DBR microcavity with two cavity modes (their wavelengths are indicated).

between)^v. The cavity modes are calculated as follows: For a resonant cavity mode and for an arbitrary point inside the cavity, light passed i and light passed j round trips inside the cavity should interfere constructively. From equation (2.3), this leads, under the assumption that the phase shift at both mirrors is the same (either both 0 or both π), to the condition

$$\begin{aligned} |\vec{k}_m| &= \frac{m\pi}{\ell_c \cos \theta_c} \\ \Leftrightarrow \omega_m &= \frac{m\pi c}{n_c \ell_c \cos \theta_c} \end{aligned} \quad (2.30)$$

for the cavity mode wave vector \vec{k}_m and angular frequency ω_m , where $m \in \mathbb{N} \setminus \{0\}$ is the *order* of the cavity mode, θ_c the angle of propagation of light inside the cavity and ℓ_c is the thickness of the cavity.

^vA DBR microcavity is not a classical microcavity because the DBRs induce a phase shift which in general is neither 0 nor π ; see equation (2.31) below.

2.6.2 Modes of DBR microcavities.

For DBR microcavities, theory is a bit more involved. Theoretical considerations about DBR microcavities were done by Panzarini et al. [7, 8]. Their results will be summarised here.

The reflection coefficient of a microcavity DBR with $n_1 > n_2$ ^{vi} is

$$r_{\text{DBR}} \approx \sqrt{\mathfrak{R}} e^{i \frac{n_c}{c} \ell_{\text{DBR}} (\omega - \omega_s) \cos \theta_c}. \quad (2.31)$$

The approximation assumes that the modulus $\sqrt{\mathfrak{R}}$ of the reflection coefficient does not depend on the light angular frequency ω , and that the phase^{vii} $\frac{n_c}{c} \ell_{\text{DBR}} (\omega - \omega_s) \cos \theta_c$ is linear in the mismatch $\omega - \omega_s$ of ω with respect to the centre of the stop band frequency ω_s . This approximation is valid for small $|\omega - \omega_s|$; i.e. for ω lying well inside the stop band. ℓ_{DBR} represents a depth of penetration of the electromagnetic field into the DBR. At $\theta = 0$, ℓ_{DBR} equals a length ℓ_τ , where ℓ_τ is the distance from the DBR surface at which a “normal” mirror must be placed so that light obtains a phase delay upon reflection at that displaced mirror equal to the phase delay upon reflection at the undisplaced DBR. \mathfrak{R} , ℓ_{DBR} , and ω_s depend on the refractive indices of the materials incorporated into the microcavity and the angle of propagation. As they also depend on the polarisation of the electromagnetic field, the amplitude and phase of the reflection coefficient are different for different polarisation directions. Expressions for \mathfrak{R} , ω_s and ℓ_{DBR} are given in the appendix of publications by Panzarini et al. [7, 8] for both polarisations; they were approximated utilising the transfer matrix method. Also note that the calculation is only valid for a large number N of material 1-material 2-pairs in the DBR. The expressions for $n_1 > n_2$

^{vi}Here, material 1 is, in contrast to the notation used by Panzarini et al. [7, 8], the material at the outside (airside) of the structure.

^{vii}This actually is the phase shift which light obtains that is reflected at a DBR. In general, it can get all values, not just 0 or π , depending on ω and the DBR parameters.

are reproduced here (ω_s was already given in section (2.5) and is thus omitted here):

$$\begin{aligned}\mathfrak{R}^{\text{TE}} &= 1 - 4 \frac{n_{\text{ext}} \cos \theta}{n_c \cos \theta_c} \left(\frac{n_2 \cos \theta_2}{n_1 \cos \theta_1} \right)^{2N}, \\ \mathfrak{R}^{\text{TM}} &= 1 - 4 \frac{n_{\text{ext}} \cos \theta_c}{n_c \cos \theta} \left(\frac{n_2 \cos \theta_1}{n_1 \cos \theta_2} \right)^{2N};\end{aligned}\tag{2.32}$$

$$\begin{aligned}\ell_{\text{DBR}}^{\text{TE}} &= \frac{2n_1^2 n_2^2 (\ell_1 + \ell_2) \cos^2 \theta_1 \cos^2 \theta_2}{n_c^2 (n_1^2 - n_2^2) \cos^2 \theta_c} \text{ and} \\ \ell_{\text{DBR}}^{\text{TM}} &= \frac{2n_1^2 n_2^2 (\ell_1 \cos^2 \theta_1 + \ell_2 \cos^2 \theta_2)}{n_c^2 (n_1^2 \cos^2 \theta_2 - n_2^2 \cos^2 \theta_1)}.\end{aligned}\tag{2.33}$$

θ_i is the angle of light propagation inside material i and n_{ext} is the refractive index of the medium surrounding the microcavity. In all further considerations, $n_{\text{ext}} = 1$ will be assumed^{viii}.

The cavity modes are determined by

$$r_{\text{DBR}}^2 e^{2i\tilde{k}_{m_z} \ell_c} = 1\tag{2.34}$$

(\tilde{k}_{m_z} is the z component of the cavity mode complex \vec{k} vector, evaluated inside the cavity layer). Because $|r_{\text{DBR}}| \leq 1$ in general, this gives complex \tilde{k}_{m_z} and thus complex cavity mode frequencies. The imaginary part of the cavity mode frequency is the spectral mode half width at half maximum, and the real part, the real cavity mode frequency, is

$$\omega_m = \frac{\ell_c \omega_c + \ell_{\text{DBR}} \omega_s}{\ell_c + \ell_{\text{DBR}}},\tag{2.35}$$

where $\omega_c = \frac{m\pi c}{n_c \ell_c \cos \theta_c}$ are the cavity mode frequencies of a “classical” microcavity (see equation (2.30)). $\ell_{\text{eff}} := \ell_c + \ell_{\text{DBR}}$ can be interpreted as an effective cavity thickness.

^{viii}In reality, a glass substrate is used for the experiments described in chapters (5) and (4), thus $n_{\text{ext}} \approx 1.45$ at one side and $n_{\text{ext}} = 1$ at the other side of the cavity. However, this does not play a role for the qualitative effects, and since no precision measurements were done, this can be ignored when doing the theory where the physical effects as such are important. In fact, when performing transfer matrix calculations resembling the experiments, the glass substrate is taken into account.

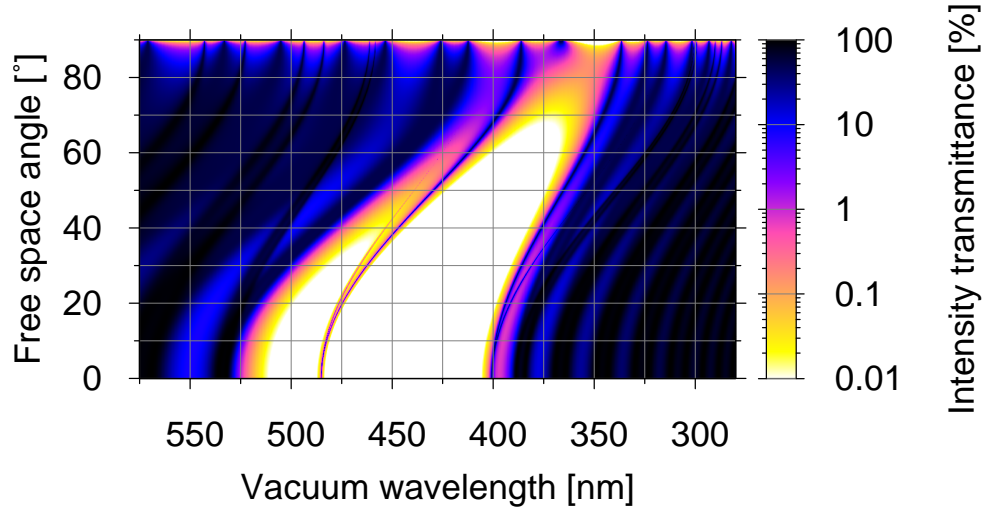


Figure 2.9: Angle resolved transmission spectrum of a DBR microcavity. Plotted is the intensity transmittance of the cavity in % in logarithmic scale. The white region in the centre is the stop band, where two cavity modes can be seen, one at the small wavelength edge, the other in the left third of the stop band. The plot shows the angular dispersion of the cavity mode. The data for angles close to 90° are probably not correct anymore since the numerics diverges and degenerates for $\theta \rightarrow 90^\circ$. Also, a splitting of the cavity modes for angles $> 0^\circ$ can be seen. This is polarisation splitting and will be explained in section 2.6.3. This spectrum is calculated with the software FilmWizard [6] from Scientific Computing International, utilising the transfer matrix method.

Angle Dependence of the Mode Frequency.

The angle dependence of the cavity mode frequency is simple in the case when the refractive indices of the mirror and cavity layer materials are close to each other; this is the approximation $n_1 \approx n_2 \approx n_c =: n_{\text{eff}}$. This approximation yields $\theta_1 \approx \theta_2 \approx \theta_c =: \theta_{\text{eff}}$ via $n_1 \sin \theta_1 = n_2 \sin \theta_2$, and $\ell_1 \approx \ell_2$ via equation (2.26). Note that under this approximation ℓ_{DBR} diverges (see equation (2.33)), and from equation (2.35) it follows $\omega_m \approx \omega_s$. A look at equation (2.29) then reveals the angle dependence of the cavity mode frequency:

$$\frac{\omega_m(\theta_{\text{eff}})}{\omega_m(0^\circ)} \approx \frac{1}{\cos \theta_{\text{eff}}}. \quad (2.36)$$

For the wavelength, this yields with $\lambda = \frac{2\pi c}{n\omega}$,

$$\frac{\lambda_m(\theta_{\text{eff}})}{\lambda_m(0^\circ)} \approx \cos \theta_{\text{eff}}. \quad (2.37)$$

If the refractive indices of the material differ, the analytical calculation of the angular dispersion is more involved, but the result is qualitatively similar.

Figure 2.9 shows the calculated dispersion of the cavity mode for the following DBR microcavity: The DBRs are identical to those whose transmission spectrum is depicted in figure 2.6, the parameters for the cavity layer are $n_c = 1.7$ and $\ell_c = 528.75 \text{ nm} = 4.7 \frac{\lambda_s}{4}$.

2.6.3 Polarisation splitting in DBR microcavities.

Since ℓ_{DBR} and ω_s are polarisation dependent, the cavity mode frequency will be slightly different for both, TE and TM, polarisations; whereas the difference of \Re for both polarisations results in a difference of the cavity mode half width. The effect of differing mode frequencies will be discussed here.

Panzarini et al. [7, 8] consider the case at which n_1 , n_2 and n_c are close to each other. Then, ω_s is approximately the same for both polarisations and only ℓ_{DBR} makes up the polarisation difference of the cavity mode frequency. The *polarisation splitting* Δ of the mode frequencies is given in those approximations as

$$\Delta(\theta) := \omega_m^{\text{TM}}(\theta) - \omega_m^{\text{TE}}(\theta) \simeq \frac{\ell_c \left(\ell_{\text{DBR}}^{\text{TM}}(\theta) - \ell_{\text{DBR}}^{\text{TE}}(\theta) \right) (\omega_s(0^\circ) - \omega_c(0^\circ))}{(\ell_c + \ell_{\text{DBR}}(0^\circ))^2 \cos \theta_{\text{eff}}}. \quad (2.38)$$

The polarisation splitting is zero for $\theta = 0$ (which generally has to be the case because at $\theta = 0$ the polarisations are not distinguishable) as well as for $\omega_s = \omega_c$.

ω_c and ω_s are approximately equivalent (exactly for $\theta = 0$) if $n_c \ell_c = 2mn_i \ell_i$, $m \in \mathbb{N} \setminus \{0\}$. Furthermore, for $\omega_c = \omega_s$, it is $\omega_m = \omega_c$ (refer to equation (2.35)). Sometimes the quantity $\omega_s(0^\circ) - \omega_c(0^\circ)$, sometimes $\omega_s(0^\circ) - \omega_m(0^\circ)$ is called the *detuning* Γ of the cavity. Here, $\Gamma = \omega_s(0^\circ) - \omega_m(0^\circ)$ will be used, since ω_m is experimentally directly accessible^{ix} whilst ω_c is not. To see how ω_m and ω_c are related, a look at equation (2.35) helps: Expressing all occurrences of ℓ_c in terms of ω_c , it is obvious that ω_m grows iff ω_c grows; the same holds true for shrinking frequencies. Furthermore, ω_m lies between ω_c and ω_s . For $\ell_{\text{DBR}} \rightarrow 0$, $\omega_m \rightarrow \omega_c$, conversely, for $\ell_{\text{DBR}} \gg \ell_c$, $\omega_m \rightarrow \omega_s$. So, $\omega_s(0^\circ) - \omega_m(0^\circ)$ is zero if $\omega_s(0^\circ) - \omega_c(0^\circ)$

^{ix}At least in the experiments laid out in this work ω_m is directly measured whereas ω_c is not.

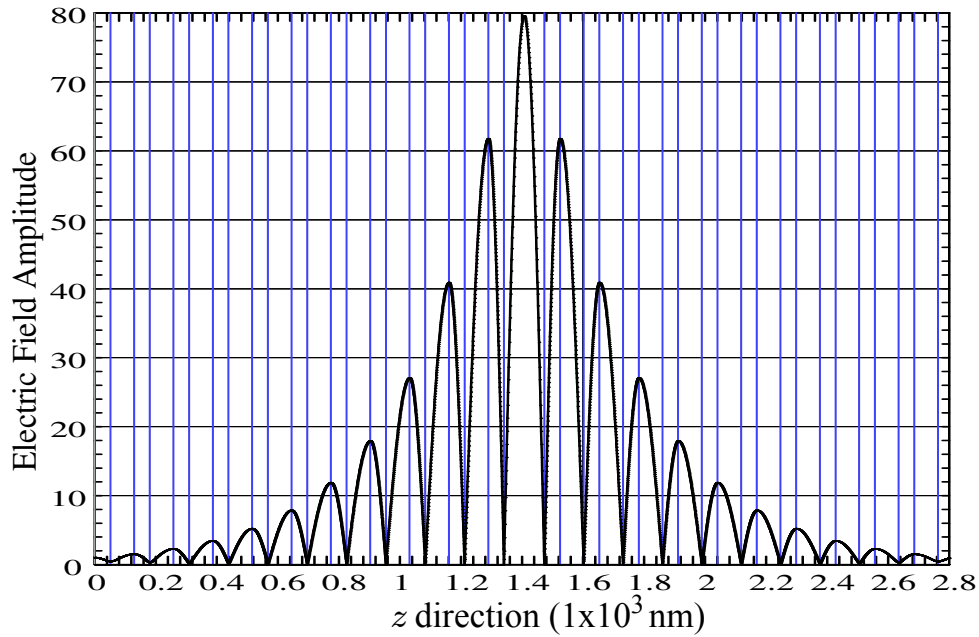


Figure 2.10: Electric field amplitude in a DBR microcavity depending on the depth inside the sample. The cavity is illuminated from the left side with a wavelength corresponding to the cavity ground mode ($m = 1$) wavelength $\omega_m(0^\circ)$. The electric field amplitude is normalised such that the incident field has an amplitude of 1. The vertical lines are not the coordinate grid but indicate the boundaries between the material layers. In the centre, around 1400 nm, the cavity layer is visible as the thickest layer in the structure. The field is calculated using a software (SCI FilmWizard, [6]) which utilises the transfer matrix method.

is zero, and both quantities simultaneously grow or shrink. Γ lies always between zero and $\omega_s(0^\circ) - \omega_c(0^\circ)$.

From equation (2.38), it directly follows that the polarisation splitting approximated as above linearly depends on $\omega_s(0^\circ) - \omega_c(0^\circ)$. It will be zero for $\Gamma = 0$ and grow and shrink with Γ , but, in general, does not exactly linearly depend on Γ .

2.6.4 Electromagnetic field enhancement in microcavities.

For resonant frequencies, the electromagnetic field inside the cavity is much higher than the field outside. A calculation of this field enhancement effect is shown in figure (2.10). If the cavity layer is filled with an optically active medium, this field enhancement effect

enhances the coupling between the atoms or molecules in the medium and the cavity mode.

Experimental studies on the polarisation splitting are presented in chapter 4. The dependence of the splitting on the detuning of the cavity mode is directly measured using a sample which has a thickness gradient incorporated into the cavity layer. The results are compared to transfer matrix calculations and to the approximate analytical equation (2.38). It is found that for oblique angles the cavity mode splits into two modes and that the splitting increases with the detuning. The modes are well orthogonally polarised. The results agree with the theory.

2.7 Fabry-Pérot Interferometer. Angular Dependent Cavity Transmission Spectrum.

In this section, the resonance properties of a simple Fabry-Pérot interferometer are analytically reviewed. This framework will then be applied to DBR microcavities, yielding an analytical approximation for angle- and frequency-dependent DBR microcavity resonance.

A *Fabry-Pérot interferometer* essentially is some space bound by two plane parallel (partly) reflective surfaces with a distance ℓ_{fp} between them. So, a Fabry-Pérot interferometer can be understood as a cavity with surface reflecting mirrors (compare with the paragraph on “classical” cavities on page 27). The thickness ℓ_{fp} of the interferometer is the quantity ℓ_{c} —the cavity thickness—used in equation (2.30), which will be used from now on instead of ℓ_{fp} . See figure 2.11 for the beam propagation inside a Fabry-Pérot interferometer. The mirrors of the interferometer can be just a single material boundary, so the device may be constructed by taking a plate of a transparent material and placing it in air.

The spectral and angular transmittance and reflectance of a Fabry-Pérot interferometer are described by the so-called *Airy formulae* [2]. In a book by Born and Wolf [2], the derivation of the Airy formulae is given for an interferometer with identical mirrors. They

are:

$$\begin{aligned} I_r &= \frac{4\mathcal{R} \sin^2 \frac{\delta}{2}}{(1 - \mathcal{R})^2 + 4\mathcal{R} \sin^2 \frac{\delta}{2}} I_i = \frac{1}{1 + \frac{1}{F \sin^2 \frac{\delta}{2}}} I_i \text{ and} \\ I_t &= \frac{\mathcal{T}^2}{(1 - \mathcal{R})^2 + 4\mathcal{R} \sin^2 \frac{\delta}{2}} I_i = \frac{1}{1 + F \sin^2 \frac{\delta}{2}} I_i, \end{aligned} \quad (2.39)$$

where I_i , I_r , and I_t are the intensities of the incident, reflected, and transmitted wave, respectively, $F = \frac{4\mathcal{R}}{(1-\mathcal{R})^2}$ is the *finesse* coefficient of the cavity, and the relation $\mathcal{T} = 1 - \mathcal{R}$ (see equation (2.13)) is used to introduce F . Before explaining the remaining symbols in these equations, the corresponding equations^x for the complex electric amplitudes will be given, since they will be used later on:

$$\begin{aligned} A_r &= \frac{(1 - e^{i\delta}) \sqrt{\mathcal{R}}}{1 - \mathcal{R}e^{i\delta}} A_i \text{ and} \\ A_t &= \frac{\mathcal{T}}{1 - \mathcal{R}e^{i\delta}} A_i. \end{aligned} \quad (2.40)$$

Here, A_i , A_r , and A_t are the electric complex amplitude of the incident, reflected, and transmitted wave, respectively, and δ is the phase a wave accumulates while traversing the cavity twice. $\mathcal{T} = t\tilde{t}$, $\mathcal{R} = r^2$, where t and r are the complex transmission and reflection coefficients, respectively, of the mirrors for light travelling from the mirrors into the cavity.

^xAlso taken from [2].

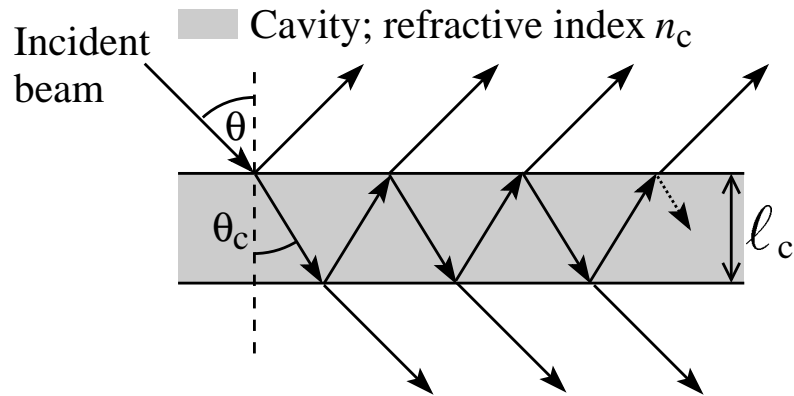


Figure 2.11: Beam propagation in a Fabry-Pérot plate, surrounded by vacuum.

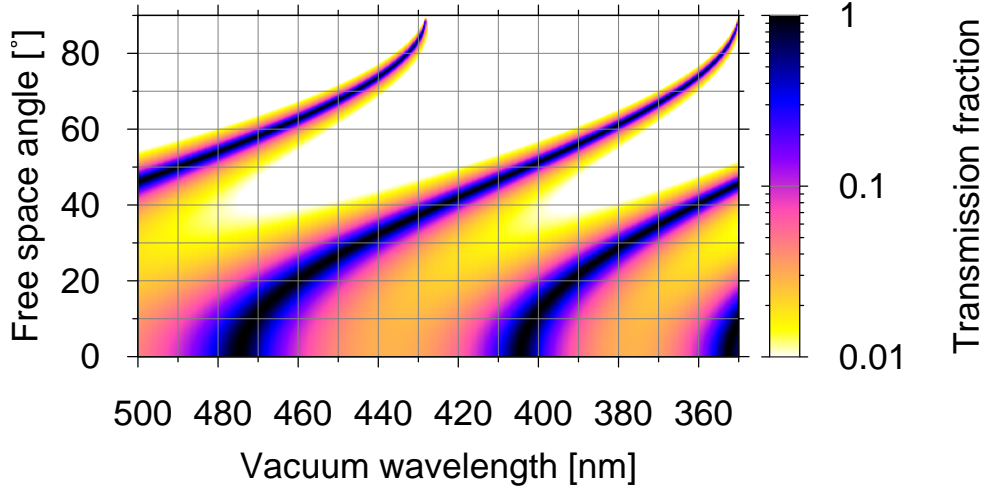


Figure 2.12: Wavelength and angle dependent intensity transmittance $\frac{I_t}{I_i}$ of a DBR microcavity, calculated according to equation (2.44). Note that only for $\lambda \approx \lambda_s = 417.5$ nm the values are exact (see text before equation (2.44)).

Conversely, \tilde{t} and \tilde{r} are the transmission and reflection coefficients, respectively, at the mirror-cavity-boundary for light travelling from the cavity to the mirrors. δ is given by [2]

$$\delta = \frac{2\omega}{c} n_c \ell_c \cos \theta_c. \quad (2.41)$$

Substituting equation (2.41) into (2.40), one obtains the frequency and angle dependent reflection and transmission:

$$\begin{aligned} A_r &= \frac{\left(1 - e^{i\frac{2\omega}{c} n_c \ell_c \cos \theta_c}\right) \sqrt{\mathcal{R}}}{1 - \mathcal{R} e^{i\frac{2\omega}{c} n_c \ell_c \cos \theta_c}} A_i \text{ and} \\ A_t &= \frac{\mathcal{T}}{1 - \mathcal{R} e^{i\frac{2\omega}{c} n_c \ell_c \cos \theta_c}} A_i. \end{aligned} \quad (2.42)$$

From this, the cavity mode frequencies can be calculated as the frequencies of maximum transmission.

To apply equations (2.40) and (2.41) to DBR microcavities, the phase shift that light obtains when it is reflected at the DBRs, must be considered: \mathcal{R} in equation (2.40) must be replaced by \mathcal{R}_{DBR} , where $\mathcal{R}_{\text{DBR}} := r_{\text{DBR}}^2 \approx \Re e^{i2\frac{n_c}{c} \ell_{\text{DBR}} (\omega - \omega_s) \cos \theta_c}$

($r_{\text{DBR}} \approx \sqrt{\Re} e^{i \frac{n_c}{c} \ell_{\text{DBR}} (\omega - \omega_s) \cos \theta_c}$ from equation (2.31)). For the transmission^{xi}, this leads to

$$A_t \approx \frac{\mathcal{T}}{1 - \mathcal{R}_{\text{DBR}} e^{i \frac{2\omega}{c} n_c \ell_c \cos \theta_c}} A_i = \frac{\mathcal{T}}{1 - \Re e^{i 2 \frac{n_c}{c} (\ell_{\text{DBR}} (\omega - \omega_s) + \ell_c \omega) \cos \theta_c}} A_i. \quad (2.43)$$

This equation is only valid for angular frequencies ω close to the frequency ω_s of the centre of the DBR stop band, since this approximation was used in the equation for r_{DBR} . The transmission intensity is then given by

$$I_t = A_t A_t^* \approx \frac{\mathcal{T}^2}{1 + \Re^2 - 2\Re \cos \left(2 \frac{n_c}{c} (\ell_{\text{DBR}} (\omega - \omega_s) + \ell_c \omega) \cos \theta_c \right)} I_i. \quad (2.44)$$

The angle and spectrally dependent transmission $\frac{I_t}{I_i}$ according to equation (2.44) is shown in figure 2.12. For calculating the data for this figure, the following parameters were used: $n_1 = 1.45$, $n_2 = 2.19$, $n_c = 1.75$, $\lambda_s = 417.5 \text{ nm}$, $n_1 \ell_1 = n_2 \ell_2 = \frac{\lambda_s}{4}$, $\ell_c = 4.7 \cdot \frac{\lambda_s}{4}$; \Re and ℓ_{DBR} were calculated for TE polarisation according to equation (2.32) and (2.33) with $N = 2.5$ and $n_{\text{ext}} = 1$, ω_s was calculated for TE polarisation with equation (2.29). N was chosen relatively small to achieve a broad, well visible resonance line in the figure.

The cavity mode frequencies ω_m are at the maxima of the cavity transmission intensity:

$$\begin{aligned} 2 \frac{n_c}{c} (\ell_{\text{DBR}} (\omega - \omega_s) + \ell_c \omega_m) \cos \theta_c &= 2m\pi \quad (m \in \mathbb{N}) \\ \Rightarrow \omega_m &= \frac{m\pi c}{(\ell_c + \ell_{\text{DBR}}) n_c \cos \theta_c} + \frac{\ell_{\text{DBR}}}{(\ell_c + \ell_{\text{DBR}})} \omega_s. \end{aligned} \quad (2.45)$$

This reproduces the result already known from equation (2.35).

2.8 Effective Reflectance.

In reality, the cavity medium is absorbing, and when it is optically pumped it can also have gain. For the discussion of the resonance characteristics, these effects can be incorporated into the mirror reflectivities, yielding effective reflectivities. This is laid out here.

Let the absorption coefficient of the cavity layer be given by α and the gain constant of the pumped cavity medium by g .

^{xi}The reflection will not be considered further since the cavity mode can be determined by the transmission maximum.

The electromagnetic field does not only propagate inside the cavity layer, but also shows some overlap with the mirror layers (and the outside, if the mirrors are thin enough). In general, absorption and gain are material dependent, too. So, α and g will be understood in an averaged manner as follows: For ideally reflecting mirrors ($|r_{\text{DBR}}| = 1$), during one round trip of the light inside the cavity with effective cavity length ℓ_{eff} , the amplitude of the light is damped (or enhanced, iff $g > \alpha$) by a factor of^{xii} $e^{-(\alpha-g)2\frac{\ell_{\text{eff}}}{\cos\theta_c}}$. For this definition it is assumed that α and g are homogeneously distributed in the x - y -direction (at least in the region penetrated by the electromagnetic field). The quantity

$$\bar{\alpha} := \alpha - g \quad (2.46)$$

will be called the *effective absorption constant* of the cavity material.

In general, the mirrors are not ideally reflective, but have a reflection coefficient with modulus r_i (where $i \in \{1, 2\}$ indexes the two mirrors of the cavity), $r_i \leq 1$. Therefore, during one round trip, the amplitude is additionally damped by $r_1 r_2$. Putting both effects—material effective absorption and mirror losses—together, the amplitude gets damped (or enhanced) by a factor

$$\bar{r}^2 := r_1 r_2 e^{-2\bar{\alpha}\frac{\ell_{\text{eff}}}{\cos\theta_c}} \quad (2.47)$$

during one round trip. $\bar{r}_i := r_i e^{-\bar{\alpha}\frac{\ell_{\text{eff}}}{\cos\theta_c}}$ will be called the *effective reflection coefficient* of mirror i .

The idea of introducing the absorption into the description of the cavity resonance by modifying the reflection coefficient with an absorption factor $e^{-\alpha\frac{\ell_{\text{eff}}}{\cos\theta_c}}$ was laid out by Enomoto et al. [9]^{xiii}. Björk et al. [10] introduced the idea of the effective absorption $\alpha - g$, so including gain by a factor $e^{g\frac{\ell_{\text{eff}}}{\cos\theta_c}}$ is a further improvement in the description of cavities with loss *and* gain.

^{xii}The factor “2” in front of ℓ_{eff} is there because one round trip involves travelling ℓ_{eff} twice.

^{xiii}With the difference, that Enomoto et al. [9] introduced the absorption of a material in form of a damping constant for the intensity, whereas here it is introduced as a damping constant for the amplitude.

2.9 Cavity Mode Radius.

In a real cavity, the cavity modes have a finite spatial extension along the cavity plane. This section deals with the introduction of a measure of the in plane radius of cavity modes. At the end, the dependence of the mode radius on the absorption and gain of the cavity medium is discussed.

In a cavity without loss and which extends infinitely in the x - y -plane, the \vec{k} vector and thus the momentum $\hbar\vec{k}$ of the photon field is defined sharply. The cavity photon field therefore delocalises along the x - y -plane [11]. In a damped cavity, a cavity photon has a finite lifetime and thus a non-zero energetic width $\hbar\Delta\omega$. The momentum the field has a width $\hbar\Delta\vec{k}$, and the propagation direction a width $\Delta\theta$. A single cavity photon is therefore localised within the cavity plane, with some characteristic spatial uncertainty Δx . This localisation defines a *radius* of the cavity mode.

The intensity of a mode does not fall off abruptly at its radius, but decreases gradually within the x - y -plane. Thus, a mode radius can not rigorously be defined. Rather, one has to find some characteristic radius.

Moreover, in a cavity which is weakly and homogeneously(!) excited, one would not observe discrete localised modes. Rather, each photon will have its own localisation determined by the mode radius, the next photon can already be localised at a slightly different position. That is why sometimes the term *quasimode* is used for the spatial modes in planar microcavities.

Amongst others, De Martini et al. [11], Björk et al. [10] and Ujihara [12] made considerations on the size of the cavity modes in the x - y -plane of an infinitely extending microcavity. The way Björk et al. [10] derived an expression which characterises the radius of one coherent mode will be followed here, while introducing some minor changes:

Equation (2.37) approximates the angle dependence of the cavity mode wavelength in a DBR microcavity. Taylor expansion of the quantity $\lambda_m(0^\circ) - \lambda_m(\theta_c)$ with respect to θ_c up to quadratic order^{xiv} yields $\lambda_m(0^\circ) - \lambda_m(\theta_c) \approx \frac{1}{2}\lambda_m(0^\circ)\theta_c^2$. Of course, this Taylor

^{xiv}In contrast to equation (2.37), θ_c is used here instead of θ_{eff} . This is justified because in the case where θ_{eff} is defined exactly, $\theta_c = \theta_{\text{eff}}$, otherwise using θ_c is quite precise since the light inside the cavity layer is of most interest (the best would be to take a mixture of θ_c , θ_1 and θ_2 weighted with the light penetration). In fact, equation (2.37) is only approximately valid, since in a real DBR microcavity the refractive indices of the different materials have to be different for the device to function, which was neglected for its derivation.

expansion assumes small values of θ_c and, thus, also small values of θ . Using the law of refraction ($n_c \sin \theta_c = \sin \theta$), and omitting the sine function since the angles are assumed to be sufficiently small, the dispersion of the cavity mode wavelength for small vacuum angles θ is obtained:

$$\lambda_m(0^\circ) - \lambda_m(\theta) \approx \frac{\lambda_m(0^\circ)}{2n_c^2} \theta^2. \quad (2.48)$$

The quadratic dependence of $\lambda_m(0^\circ) - \lambda_m(\theta)$ on θ for small θ is directly visible in the figures 2.9 and 4.4.

Björk et al. [10] approached λ_m by taking a simplified version of the condition expressed in equation (2.34):

$$e^{2ik_{m_z}\ell_c} = 1, \quad (2.49)$$

which leads to real values for k_{m_z} (λ_m is obtained by $\lambda = \frac{2\pi n_c \cos \theta_c}{k_z}$)^{xv}. This derivation holds true for wavelengths very close to the wavelength of the centre of the DBR stop band; in this spectral region, the reflection coefficient r_{DBR} of the DBR mirrors is real, and the condition (2.49) yields correct k_m . In fact, Björk et al. [10] performed the derivations presented here under the assumptions $\omega \approx \omega_s$ and r_{DBR} being real.

They further argue that r_{DBR} can be expressed explicitly in terms of k_z and θ_c only and depends only slightly on the angle for small θ_c . Hence, for incidence around the normal direction and for cavity modes close to the centre of the stop band, the resonance characteristics are given by k_z only. This implies that changing k_z via a small change in θ and keeping the wavelength constant changes the resonance condition in the same way as changing k_z by varying $|\vec{k}| = \frac{2\pi}{n_c \lambda}$ (and thus changing the wavelength) and keeping the incidence angle constant, as long as the change of k_z is the same in both cases. (2.50)

This result will be used later to relate a spectral mode width, expressed in terms of Δk_{m_z} , to an angular mode width, expressed in terms of $\Delta \theta$.

The amplitude transmittance $\frac{A_t}{A_i}$ of a DBR microcavity is given by the Airy formula, equation (2.43). Since the reflection coefficient of the mirrors is real under the assumption $\omega \approx \omega_s$, it is given by $\sqrt{\mathfrak{R}}$ only. Instead of strictly following the derivation of Björk et al. [10], the absorption and gain as discussed in section 2.8 will be incorporated into the mirror reflectance. Additionally, $\mathcal{T} = 1 - \mathcal{R}$ (see equation (2.13) together with (2.12)) will be used to fully incorporate the absorption. The amplitude transmittance of the cavity

^{xv}Note, that the \vec{k} -vectors are given inside the cavity layer, whereas the wavelengths are vacuum wavelengths.

near the centre of the DBR stop band then becomes^{xvi}

$$\frac{A_t}{A_i} \approx \frac{1 - \Re e^{-2\bar{\alpha} \frac{\ell_{\text{eff}}}{\cos \theta_c}}}{1 - \mathcal{R}_{\text{DBR}} e^{-2\bar{\alpha} \frac{\ell_{\text{eff}}}{\cos \theta_c}} \Big|_{\omega=\omega_s} e^{i \frac{2\omega}{c} n_c \ell_c \cos \theta_c}} = \frac{1 - \bar{\Re}}{1 - \bar{\Re} e^{i 2k_z \ell_c}}, \quad (2.51)$$

where $\bar{\Re} := \Re e^{-2\bar{\alpha} \frac{\ell_{\text{eff}}}{\cos \theta_c}}$. The spectral mode width (full width at half maximum, *FWHM*) of this transmittance is [10], expressed in k_z ,

$$\Delta k_z = \frac{1 - \bar{\Re}}{\ell_c \sqrt{\bar{\Re}}}, \quad (2.52)$$

where $k_{m_z} \pm \frac{1}{2} \Delta k_z$ are the k_z values at which $\frac{A_t}{A_i}$ has fallen off to half of the value it has at $k_z = k_{m_z}$. By sentence (2.50), this corresponds to a specific spread $\Delta \theta$ in vacuum angle. It will be calculated using relation (2.48): First, the spread in wavelength corresponding to Δk_z is

$$\Delta \lambda = \frac{2\pi}{n_c |\vec{k}|^2} \Delta k = \frac{\lambda_m^2(0^\circ) (1 - \bar{\Re})}{2\pi n_c \ell_c \sqrt{\bar{\Re}}}. \quad (2.53)$$

Now, since cavity modes around the normal propagation direction are considered, the $\Delta \lambda$ corresponding to $\Delta \theta$ is given by $\frac{1}{2} \Delta \lambda = \lambda_m(0^\circ) - \lambda_m(\frac{1}{2} \Delta \theta)$. So, with equation (2.48), $\Delta \theta$ follows to be

$$\Delta \theta \approx \sqrt{\frac{4n_c^2 \Delta \lambda}{\lambda_m(0^\circ)}} = \sqrt{\frac{2n_c \lambda_m(0^\circ) (1 - \bar{\Re})}{\pi \ell_c \sqrt{\bar{\Re}}}}. \quad (2.54)$$

This equation gives the angular FWHM $\Delta \theta$ of the cavity transmission mode around normal incidence and for cavity mode wavelengths λ_m near the centre of the DBR stop band.

The isotropy of the cavity in the x - y -plane dictates that the cavity modes are isotropic, too. Thus, their spatial extent is characterised by a *mode radius* d only. To estimate d , Björk et al. [10] assume that over the whole extent of the mode in the cavity plane, the electromagnetic field is equally strong, thus resembling a uniformly illuminated circle with radius d . They use the relation for the angle dependent intensity distribution for such a circle: $I(\theta) = \left(\frac{2J_1(kd \sin \theta)}{kd \sin \theta} \right)^2 I(0^\circ)$, where J_1 is the first Bessel function of the first kind. For θ they use the angle $\frac{\Delta \theta}{2}$ at which the intensity drops off to half its maximum

^{xvi} $k_z = \frac{n_c \omega}{c} \cos \theta_c$ has been used.

value^{xvii}. With that, they deduce the mode radius to be $d \approx \frac{\lambda_m(0^\circ)}{2\Delta\theta}$, where several numerical approximations have been used in order to solve for the Bessel and the sine function. Using equation (2.54), the mode radius can be estimated by

$$d \approx \sqrt{\frac{\pi \lambda_m(0^\circ) \ell_c \sqrt{\bar{\mathfrak{R}}}}{8n_c(1 - \bar{\mathfrak{R}})}}. \quad (2.55)$$

The parameter $\frac{4\bar{\mathfrak{R}}}{(1-\bar{\mathfrak{R}})^2}$ is the effective^{xviii} cavity *fineness coefficient* and will be denoted by \bar{F} . The equation (2.55) improves the expression originally derived by Björk et al. [10] by taking into account absorption and gain within $\bar{\mathfrak{R}}$ and \bar{F} .

This result for the mode radius is a qualitative result; other derivations lead to similar results with other numerical factors. For example, another derivation by Björk et al. [10], utilising the density of modes, leads to

$$d \approx \sqrt{\frac{\lambda_m(0^\circ) \ell_c \sqrt{\bar{\mathfrak{R}}}}{\pi n_c(1 - \bar{\mathfrak{R}})}}. \quad (2.56)$$

De Martini et al. [11] derive a distance over which a coupling via stimulated emission of individual places within the cavity can take place, which is a measure for the mode diameter $2d$, and they obtain

$$d \approx \sqrt{\frac{2\pi \lambda_m(0^\circ) \ell_c \sqrt{\bar{\mathfrak{R}}}}{n_c \mathcal{T}(1 - \bar{\mathfrak{R}})}}. \quad (2.57)$$

If both mirrors have a different reflectance (but the centre of the stop band at the same wavelength), this can be accounted for by setting $\bar{\mathfrak{R}} = \sqrt{\mathfrak{R}_1} \sqrt{\mathfrak{R}_2} e^{-2\bar{\alpha} \frac{\ell_{\text{eff}}}{\cos \theta_c}}$, where $\sqrt{\mathfrak{R}_i} = r_{\text{DBR}_i}|_{\omega=\omega_s}$ is the reflection coefficient of mirror i for $\omega = \omega_s$.

Looking at equation (2.55), one can see that the mode radius will grow as $\bar{\mathfrak{R}}$ approaches unity. In real cavities, $\bar{\mathfrak{R}}$ is smaller than one due to mirror losses and material absorption. However, by inducing gain this can be compensated, making the mode radius growing. Theoretically, if the gain exactly compensates material and mirror losses, i.e. if $\bar{\mathfrak{R}} = 1 \Rightarrow$

^{xvii}Note: previously, Björk et al. [10] did use the FWHM of the amplitude, now they use the FWHM of the intensity.

^{xviii}Effective, because it contains absorption and gain.

$g = \alpha + \frac{\cos \theta_c}{2\ell_{\text{eff}}} \ln \frac{1}{\Re}$, the mode radius will be infinite^{xix}.

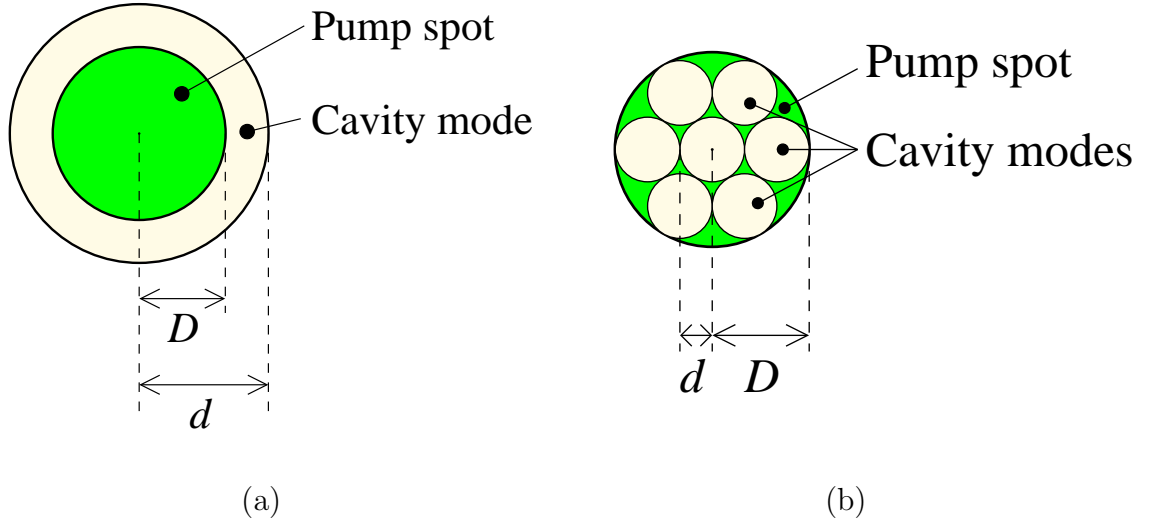


Figure 2.13: Illustration of the spatial extent of the cavity modes in the cavity plane in the case of (a) the pump spot radius D being smaller than the mode radius d , (b) D being much larger than d . In the case (b), multiple modes form. Note that the figures are only a schematic illustration, in reality, especially in the case (b), the modes will not line up so perfectly and discrete as shown in the figure. Rather, there will be a superposition of all possible spatial cavity modes which can be excited by the pump spot. (This figure was adopted from Enomoto et al. [9].)

However, in real systems, the pump region is never infinitely large, and the considerations done so far only hold true if the effective reflectivities are homogeneous at least over the extent of the mode. This is always the case if the mode radius is smaller than the pumped spot (assuming a homogeneously distributed pump intensity across the pumped area). In this case, the cavity may be considered as operating with a number of quasimodes that fill up the pumped area [9]; see figure 2.13 (b). If, on the other hand, the pump spot size is smaller than the mode radius, there will be only one active quasimode; see figure 2.13 (a). Under weak pumping, where gain is negligible, the radius of this mode is estimated by equation (2.55). But if gain is important, the assumptions made for deriving equation (2.55) no longer hold true since \bar{F} is no longer homogeneous within one quasimode. However, the mode radius is between the limits d_0 and d_∞ , where d_0 is the

^{xix}Note: $\ln \frac{1}{\Re} \geq 1$ since $\Re \leq 1$.

mode radius for zero gain over the whole cavity area, and d_∞ would be the mode radius if over the whole cavity the gain is as high as it is inside the pumped spot.

The angular width of the emission is estimated by equation (2.54). This is true as long as there is only one mode emitting or, if several spatial modes are excited, as long as they are mutually incoherent. If modes at different places within the cavity plane emit coherently with respect to each other, interferences of the light emitted from them change the angular profile.

2.10 Spatial Mode Locking.

When several spatial cavity modes are excited and they have some overlap, they can lock their mutual phases of the electromagnetic radiation above lasing threshold. This concept is introduced here.

At the onset of lasing, the gain reaches a level where it fully compensates losses. As shown before, if the pump power, and so the gain, is homogeneously distributed over the whole area of a homogeneous cavity, the emission would take place from an infinitely large area, and the angular width of the emission would vanish for an ideal cavity. However, in real systems there is no exact homogeneity. Furthermore, in the systems studied here the spot of excitation is rather small. In this case, gain only exists inside the pumped region. The integral gain must compensate the integral loss of all regions penetrated by the lasing mode. “Integral gain”, “integral loss” refers to a weighted integral of the gain or loss, integrated over the whole cavity area and weighted with the—spatially dependent—amplitude of the electromagnetic field.

Consider the case where several spatial modes are excited below lasing threshold. The case of mode growing when going through lasing threshold can also be interpreted as a phase locking of all the spatial modes: All excited spatial modes (refer to figure 2.13 (b)) maintain their radius, but the phase of the electromagnetic radiation emitted from one mode gets a fixed value compared to the phase of the radiation emitted from the other modes. This *phase locking* of the spatial modes, also called *spatial mode locking*, leads to coherent emission from all the modes. If all modes lock in with zero phase difference, then they emit exactly in the same way and may be considered as one compound mode.

There can also be the case where the sample is excited at several distinct spots. If

the spots are close enough, such that the cavity modes of different spots overlap, they can also lock their phases above lasing threshold. This phase locking does not imply a mutual phase difference of zero, but, in fact, any fixed value is possible, depending on the distribution of the pumping power along the cavity.

The locking of overlapping modes can be explained with *stimulated emission coupling* [11]: Photons from one mode can stimulate the emission of photons in the other spatial mode, and vice versa. With this mechanism, the modes are coupled, and if the stimulated emission plays the major role for photon emission (as it does in a laser, compared to the non-lasing case where spontaneous emission prevails), the overlapping spatial modes will be coherent with respect to each other.

In chapter 5, experiments are presented where the cavity is excited at two small spots of about $3\mu\text{m}$ in diameter. Each of the spots operates in single spatial mode regime (as depicted in figure 2.13 (a)). The distance s between the spots is a few μm . If s is small enough, the modes of the two spots interact: Photons from the mode excited at one spot penetrate into the region of the mode excited by the other spot. This implies that the photons from one mode induce stimulated emission in the region of the other mode and so, above lasing threshold, both spatial modes lock to a single laser, meaning that the emission from both places is coherent. This produces one supermode with a characteristic spatial and angular emission pattern defined by the interferences of the emission from the two spots. Depending on s , the phase between the two locked modes is either 0 or π .

3 Experimental Setup.

This chapter describes the experimental setup used for conducting the experiments presented in this work.

A sketch of the experimental setup, which is used for the experiments presented in chapters 4 and 5, is depicted in figure 3.1, together with the coordinate axes used throughout this work. In the following text, labels like (1), (2) etc. are used, which refer to correspondingly labelled objects in figure 3.1.

The following light sources can be used:

- A blue emitting diode laser (1), emitting at a wavelength of 407 nm with a nominal output power of 4 mW, operating in continuous wave (cw) mode,
- a green emitting diode laser (2), emitting at a wavelength of 532 nm (frequency doubled from 1064 nm), operating in pulsed mode with 1 kHz repetition frequency, 1 ns pulse duration, and a nominal energy of 3 μ J per pulse,
- or a halogen lamp (3) for white light, used for adjustment of the sample and focussing the imaging system.

The light source is selected using flippable mirrors (4), (5). The light of the selected sources passes two filter wheels (6). These filter wheels have 6 neutral density filters each and are used to adjust the light intensity. The strength of the filters is measured in *optical density* (OD), where OD x means a weakening of the light intensity by a factor of 10^{-x} . The nominal optical densities of the filters in the filter wheels are OD 0.004, OD 0.1 to OD 0.5 in steps of OD 0.1 for one and OD 0.004, OD 0.5 to OD 2.5 in steps of OD 0.5 for the other filter wheel, allowing to set the total optical density between approximately OD 0 and about OD 3.0 in steps of approximately OD 0.1. Note that the real optical densities of the filters may differ from the nominal ones. After passing the filter wheels, the light

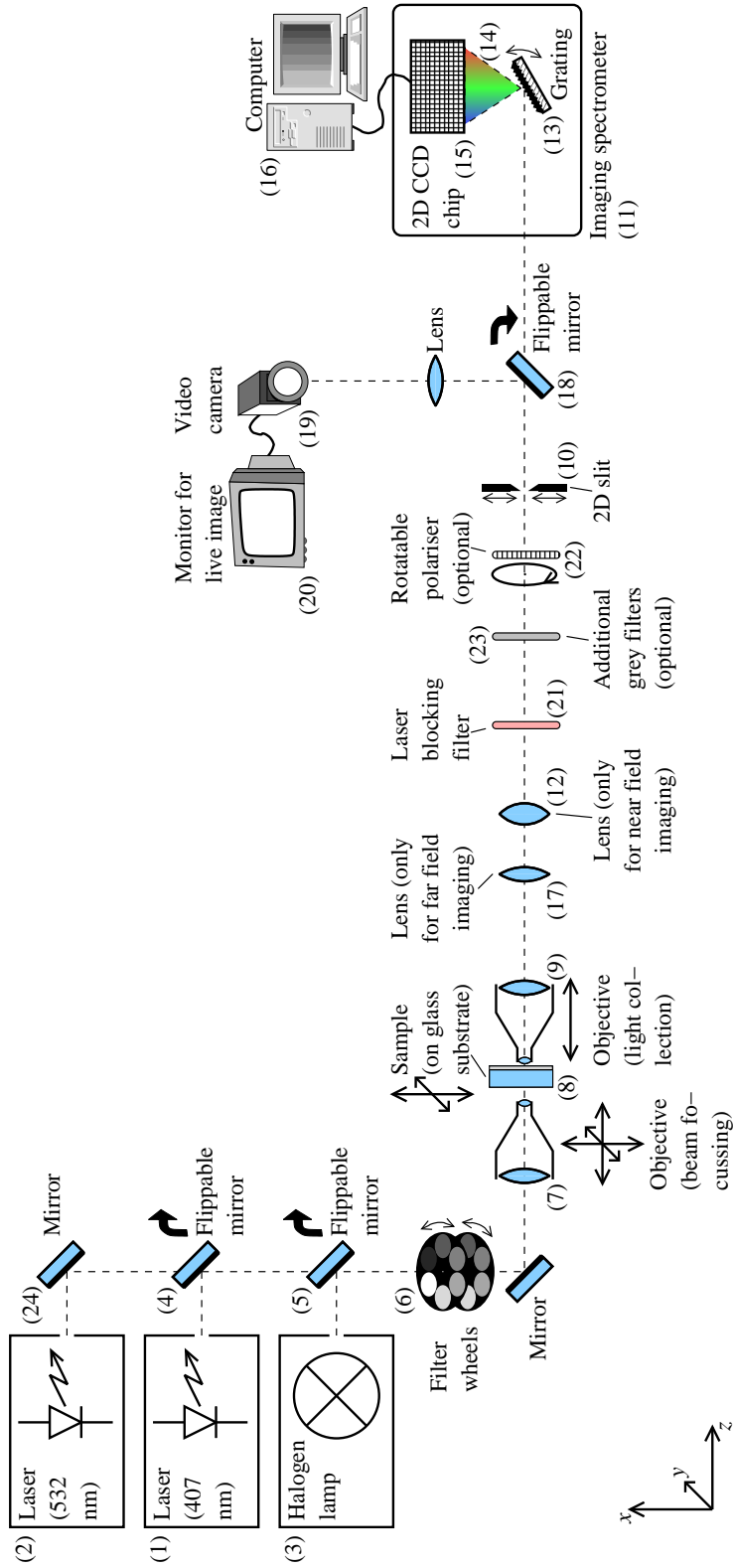


Figure 3.1: Sketch of the experimental setup. The numbers in the figure are labels referred to in the text. The coordinate axes in the lower left corner indicate the coordinate system used throughout this work.

goes through an additional grey filter (not depicted in the figure) which filters out about $\frac{3}{5}$ of the intensity, and enters an objective (7), which focuses the light onto the sample (8). The focus can be tuned by moving the objective back and forth. The laser beam has a diameter of about $3\text{ }\mu\text{m}$ in the focus point of the focussing objective. By detuning the objective, the size of the illuminated spot on the sample can be increased. The focus point can be moved in the x - y -plane by some ten μm by laterally shifting the objective. The sample is mounted on two micrometer stages which can move the sample in the x - y -plane, allowing to adjust the investigation position on the sample.

Behind the sample, another objective (9) is placed to collect the light from the sample. The numerical aperture of this objective is 0.65, which allows one to collect light from angles up to $\arcsin 0.65 \approx 40^\circ$. The focal plane of this objective is tuned to be on the investigated plane on the sample. By also adjusting the first objective, the point of illumination on the sample can be tuned to be in the focus of the second objective. The image of the light emitted from the sample can be projected in two possible regimes onto the entrance slit (10) of a spectrometer (11); the regimes will be discussed below. Before, some details about the spectrometer will be presented:

The spectrometer (Type HR 640 from Jobin Yvon) has a grating (13), which decomposes the light into its spectral components. This spectrally resolved light (14) is recorded by a two dimensional CCD chip (15) in the following way: Along one direction, where the chip has 1024 pixels, the spectral component is detected; along the other direction with 256 pixels the y direction along the entrance slit (10) is recorded. To reduce thermal noise, the CCD chip is cooled by a water cooled Peltier element. In fact, the entrance slit itself consists of two adjustable crossed slits, where one slit can crop the light in the x and the other in the y direction. In the measurement, the slits are opened such that no effects of the slits are observed in the recorded images, except shielding light that would scatter inside the spectrometer in an unexpected way. The grating of the spectrometer has 150 lines per millimetre, and it can be rotated to adjust the diffraction order and the spectral range to be projected onto the CCD chip. The actual rotation setting of the grating can be read off at the spectrometer and from this reading, the wavelength corresponding to the CCD pixels can be calculated with an empirical formula. Finally, a computer (16) controls the cooling and CCD chip and reads out the data from the chip. On the computer, these tasks are performed by the software WinSpec/32, version 2.5.15.2 from the company Roper Scientific [13]. The spectrometer itself contains other optical elements not depicted

and described here, for example lenses to image the plane of the entrance slit onto the CCD chip.

The two possible regimes of projecting the light emitted from the sample onto the spectrometer are the following:

1. In the first regime, a lens (12) is placed behind the objective (9) in such a way that the focal plane of objective (9) is projected onto the entrance slit of the spectrometer. In this way, the objective and the lens realise a microscope which projects a magnified image of the x - y -plane of the sample onto the spectrometer. This regime will be called the *near field* regime. In the near field regime the non-spectral direction of the spectrometer image has spatial resolution along the y direction of the sample.
2. In the second regime, another lens (17) is placed behind the objective (9) instead of lens (12) in order to project the Fourier transform of the sample image onto the spectrometer entrance slit. This regime will be called the *far field* regime. In this regime, different places in the plane, where the entrance slit of the spectrometer resides, correspond to different emission angles from the sample. Thus, the non-spectral direction of the spectrometer image has angular resolution for emission into the x - z -plane.

To directly observe the sample surface for alignment and adjustment, a flippable mirror (18) can be brought into the beam to direct the light onto a CCD video camera (19). This camera is connected to a TV monitor (20), which allows the experimenter a live view of the sample surface. The spatial resolution on the TV monitor is between $0.5\text{ }\mu\text{m}$ and $1\text{ }\mu\text{m}$.

When recording images with a laser as light source (1) or (2), a filter (21) is inserted into the optical path behind the sample which cuts off the short wavelength part of the spectrum, containing the laser wavelength. The emission from the sample, which is at longer wavelengths, is not affected significantly by the filter. To observe polarisation properties, a rotatable linear polarisation filter (22) can be placed in front of the spectrometer. Additionally, to weaken the light emitted from the sample, additional grey filters (23) can be put in the light path between the sample and the spectrometer. This has to be done for the lasing measurements at high excitation described in section 5.2.

With this setup, the following resolution can be reached within the spectrometer images: Spectral: Approx. 1 nm , spatial: Approx. $2\text{ }\mu\text{m}$, angular: Around 1° . The angular

and spatial resolution are limited by the pixel resolution of the CCD chip, the spectral resolution is limited by the optical system.

4 Measurement of Polarisation Splitting in planar Microcavities.

A direct measurement of the dependence of polarisation splitting in DBR microcavities on cavity mode tuning has not been reported so far. In this chapter, experimental studies of angle and mode tuning dependent polarisation splitting are presented. For the measurements, a DBR microcavity with a wedge shaped cavity layer, whose thickness increases along one direction on the sample, is used. This allows one to study different cavity resonant modes on a single same sample by just varying the position of measurement along the thickness gradient.

This chapter has three sections. Firstly, the sample and its preparation is described. Secondly, the way the experiment is conducted is presented. Thirdly, the results are presented and compared with calculations from transfer matrix theory.

4.1 The Sample.

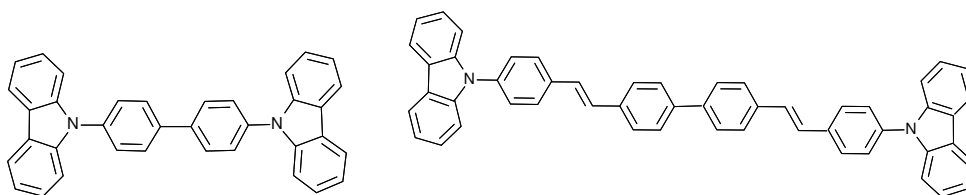


Figure 4.1: Chemical structure of CBP (left) and BSB-Cz (right).

The sample was prepared as follows: On a glass substrate, 21 layers, alternating TiO_2 and SiO_2 with TiO_2 as the first and last layer, were evaporated as the bottom DBR. Then, the cavity layer, consisting of the organic matrix material 4,4'-bis(N-carbazole)-1,1'-biphenyl (CBP, $\text{C}_{36}\text{H}_{24}\text{N}_2$) in which the dye 4,4'-bis[(N-carbazole)styryl]biphenyl (BSB-Cz,

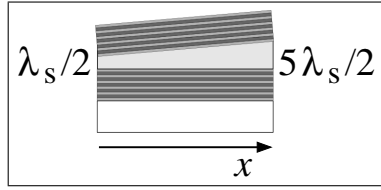


Figure 4.2: Sketch of the cross-section of the sample. At the bottom is the glass substrate, on top of which the first DBR was deposited, followed by the wedge shaped cavity layer and finished with the second DBR. The sketch is not in scale and the number of the layers does not coincide with the real number of layers.

$\text{C}_{52}\text{H}_{36}\text{N}_2$) (see figure 4.1) is embedded with a fraction of 2 weight percent as the optically active material, was grown on top of the first DBR. By using a shutter, the growth rate of the cavity layer was varied along the sample. On top of the cavity layer, the second DBR was evaporated with the same parameters as the first mirror.

The wavelength λ_s of the centre of the DBR stop band was designed to be 450 nm. Therefore the evaporation parameters were chosen such to obtain an optical thickness $n_i \ell_i$ of each mirror layer of $\frac{\lambda_s}{4} = 112.5 \text{ nm}^i$. The thickness ℓ_c of the cavity layer was designed to vary along one lateral direction (called the x -direction) from circa $\frac{450 \text{ nm}}{2}$ to circa $\frac{5 \cdot 450 \text{ nm}}{2}$ over a distance of 2.25 cm (refer to figure 4.2), leading to a slope of thickness of $\frac{d\ell_c}{dx} \approx 4 \cdot 10^{-5}$. The real values of the minimal and maximal thickness are unknown. This is not significant, since only places on the cavity well away from the thickness extrema were investigated.

Figure 4.3 shows the absorption and photoluminescence spectrum of BSB-Cz embedded into CBP with a fraction of 2 weight percent (CBP:BSB-Cz (2 wt%)). The absorption mainly occurs in CBP, and via Förster energy transfer [14] the excitation energy is non-radiatively transferred to BSB-Cz, which acts as the emitter of the system. Apparently, there is only a small overlap between the absorption and the emission spectrum. This is an advantage for the presented studies because it a) allows the system to be optically pumped outside the spectral region under investigation, therefore making it easy to block the excitation light without influencing the luminescent light much, and b) suppresses internal re-absorption of emitted light.

The host-dye-system CBP:BSB-Cz shows a low amplified stimulated emission threshold,

ⁱAnalysis of the results of optical measurements (see section 4.3) showed that the real λ_s of the finished mirrors was around 420 nm and different for different positions on the sample.

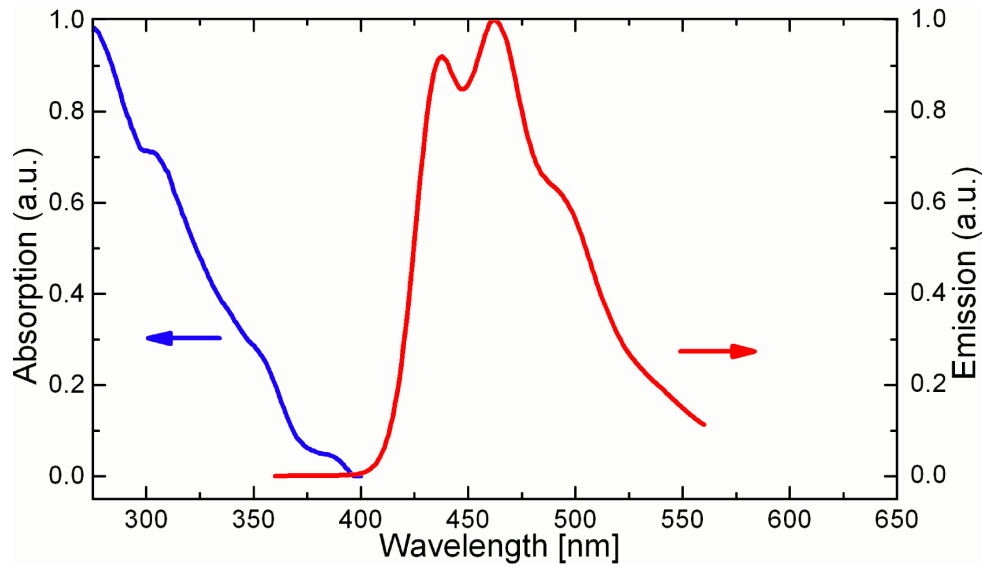


Figure 4.3: Absorption (blue, left) and emission (red, right) spectrum of CBP:BSB-Cz (2 wt%), both in separately normalised units.

$0.32 \pm 0.05 \frac{\mu\text{J}}{\text{cm}^2}$, and a high internal photoluminescence quantum efficiency [15]. It is therefore a good candidate for an organic laser. Detailed optical characteristics of this system can be found in a publication by Aimono et al. [15]. This material is new to the author's working group. Samples with CBP:BSB-Cz were fabricated in order to test how the material tends to lase in a microcavityⁱⁱ. Because the samples have a good quality, one of them is used for the polarisation splitting measurements described in this work.

Cavities with an organic active medium, like the one investigated, are a convenient tool for studying spectral cavity properties: It is possible to simultaneously select a very small region of investigation by exciting them with a well-focused laser spot and, due to their broad emission spectrum, study spectral properties over a wide range of wavelengths. Furthermore, the fact that the absorption takes place in spectral regions where there is almost no emission, the pumping can be done at wavelengths where the DBRs are transparent, while the emission spectrally lies in the DBR stop band.

ⁱⁱThese experiments were done by other persons from the working group, but they did not observe lasing yet.

4.2 The Measurement.

For the measurement, the setup described in chapter 3 is used, utilising the cw diode laser operating at a wavelength of 407 nm with a power of 4 mW (device (1) in figure 3.1). The pump power is decreased with filters far below the lasing threshold of the investigated microcavity. The pump spot is focused to a spot size of about 3 μm in diameter. Considering the wedged shape of the cavity layer, the size of the excited area leads to a variation of the cavity mode wavelength of about 0.12 nm within the excited volume, therefore the wedge shape is neglected in the evaluation of the results.

4.3 Results.

Figure 4.4 shows in the upper half subfigures ((a), (c), (e) and (g)) experimentally recorded angle resolved photoluminescence spectra. From these spectra, the wavelength $\lambda_m(\theta)$ of the cavity mode can directly be read out. The angle is only approximately calibrated (allowing for a scaling error of 30%). The splitting of the cavity mode into two modes is also directly visible. To confirm that the split modes are polarised orthogonally with respect to each other, a rotatable polarisation filter is inserted in front of the spectrometer, and images are recorded for different polariser settings. Figure 4.5 shows spectra for different polariser settings at an observation angle of about 30°. The zero degree cavity mode shown in that figure has a wavelength of $\lambda_m(0^\circ) = 482 \text{ nm}$. It clearly proves that the modes are well orthogonally polarised.

Since the measured spectra only show the long wavelength side of the microcavity stop band, it is not possible to directly identify the centre wavelength λ_s of the stop bandⁱⁱⁱ. At this point, transfer matrix calculations, carried out using the commercial software FilmWizard [6] by Scientific Computing International, come into play: The microcavity is modelled with two DBRs, both made of 21 layers of alternating materials, and a cavity layer in between. All are placed on a substrate with a refractive index of 1.45 (glass). The transfer matrix calculations are done for transmission. It is assumed that the photoluminescence spectrum of the cavity resembles its transmission spectrum, which

ⁱⁱⁱAlthough the preparation parameters were chosen to produce a cavity with $\lambda_s(0^\circ) = 450 \text{ nm}$, the preparation process is not precise enough to guarantee this, therefore the real cavity parameters have to be extracted from the measurement results. Also, the effective refractive index of the evaporated layers may differ from the refractive index of the bulk material.

is the case for an emitter with a spectrally broad emission band as the one used in the sample.

At the beginning of the transfer matrix calculations, the refractive indices for the cavity layers are set to values which have been measured in the past at thin films by other members of the author's institute. Since the refractive index of evaporated material layers may differ from sample to sample, they are adjusted in the transfer matrix model later on.

The refractive index n_1 of the layers representing TiO_2 is $n_1 \approx 2.3$ in the wavelength region of interest (around 450 nm). The refractive index decreases towards higher wavelengths. For modelling the SiO_2 layers, its refractive index is $n_2 \approx 1.46$ around 450 nm, also decreasing towards higher wavelengths. The wavelength dependence of the refractive

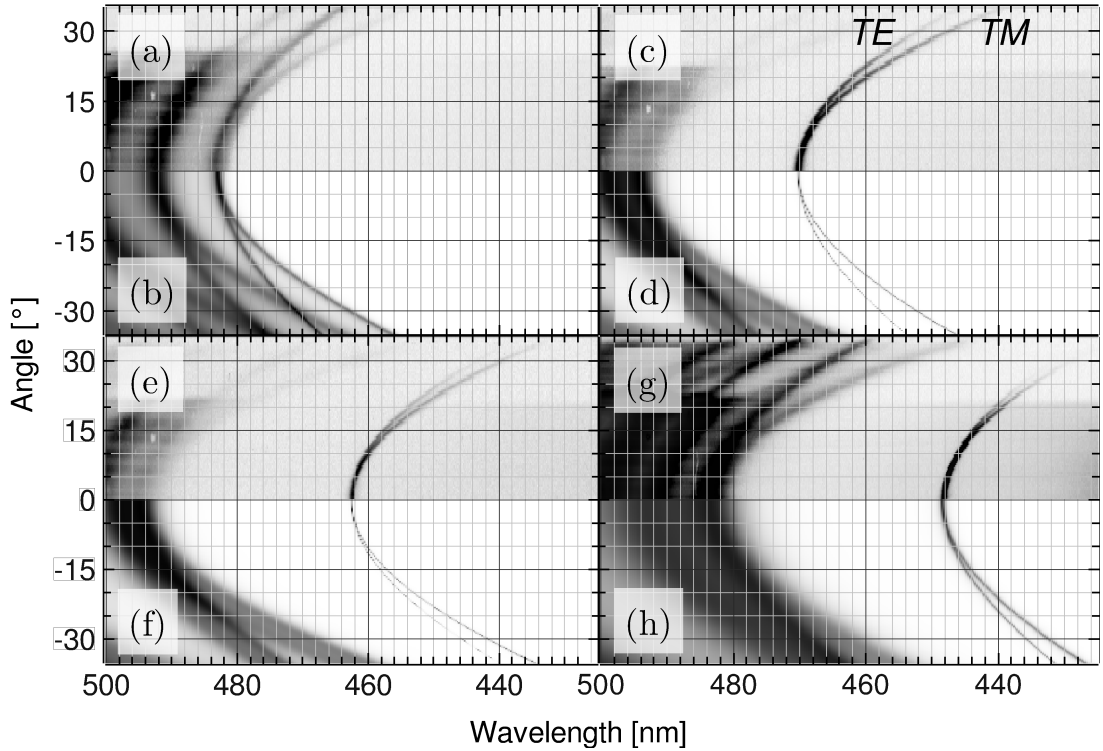


Figure 4.4: Angle resolved photoluminescence spectra of the cavity at four different cavity positions. The upper half pictures ((a), (c), (e) and (g)) show the measured results, the lower half pictures ((b), (d), (f) and (h)) results of corresponding transfer matrix calculations. The angle is the angle of propagation outside the sample. Dark paint represents high intensity, white corresponds to zero intensity.

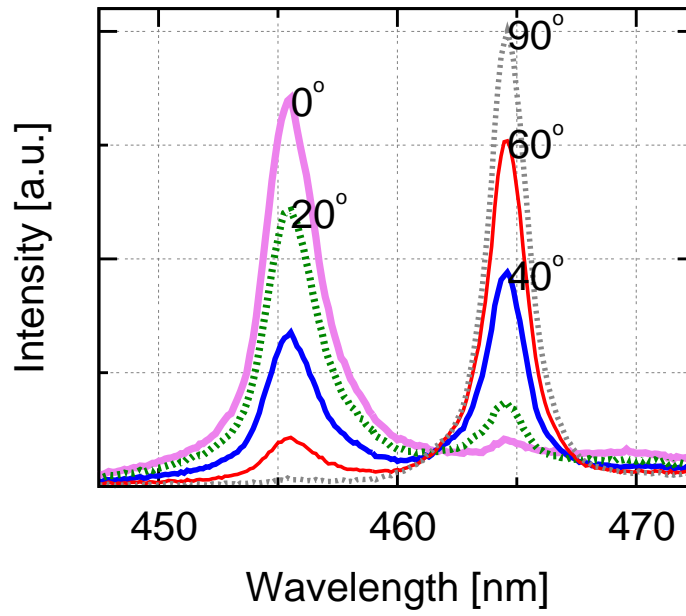


Figure 4.5: Polarisation resolved measurement of the split $\lambda_m(0^\circ) = 482 \text{ nm}$ cavity mode for an emission angle of 30° . Indicated are the relative setting angles of the polarisation filter.

indices is parametrised by the equations for a *Cauchy material* (see the manual [16] for FilmWizard, page 50). n_c , the refractive index of the cavity material, is around 1.8. n_c also decreases with increasing wavelength, but the dependence is explicitly given in a table of measurement results. Absorption is not accounted for.

The thickness of the mirror layers is set such that the optical thickness $n_i \ell_i$ of each layer is always a quarter of the wavelength λ_s of the centre of the DBR stop band.

After the model is initialised in this way, the values of λ_s , n_1 , n_2 , and the cavity layer thickness ℓ_c are varied such that the high wavelength edge of the stop band, the transmission sidebands within the stop band and the cavity mode of the transfer matrix calculations coincide with the measurement results best. During the variation, the thickness of the layers is adjusted together with their refractive index in order to keep their optical thickness constant. Since the sample properties may differ at each position, this optimisation is repeated for each single measurement. The optimisation is done by hand, by alternating and interactive adjustment of the wavelengths of the stop band, the cavity mode and the side bands outside the stop band.

This fitting procedure does not give perfect results. Also, aspects like different thicknesses of different mirror layers are not modelled. However, the result suffices to qualitatively extract the cavity thickness and centre of stop band wavelength for each measurement. The influence of the values of the refractive indices on the fitting results is comparably small. Thus, after the first good fit, they may stay constant: n_1 becomes 2.19 without wavelength dependence, n_2 remains ≈ 1.46 with dispersion as given by the initialisation of the model, and n_c becomes 1.75 without dispersion.

The fits are performed in order to obtain λ_s for the measurements. It is around 417.5 nm, but depending on the position on the sample, it usually varies between 410 nm and 425 nm, sometimes becoming even larger. The highest observed value is 432 nm. With knowing λ_s , the detuning $\Gamma_\lambda := \lambda_m(0^\circ) - \lambda_s(0^\circ)$ is known^{iv}.

The values Δ_λ of the polarisation splitting can directly be read out from the spectrometer images. Together with the values for Γ_λ , which are obtained by fitting a transfer matrix model to the measurement results as explained above, the measured polarisation splitting can be plotted versus the cavity mode detuning, which allows a comparison with the

^{iv}The index λ (or just any other available index) is important, because Γ_λ has—although describing the same physical property—a functional dependence distinct from Γ , which is defined to be the difference of the centre of stop band and cavity mode angular *frequency*.

theoretical model presented in section 2.6.3 (equation (2.38)), see figure (4.6).

The experimental results for Δ_λ are compared with results from transfer matrix calculations and theoretical predictions from equation (2.38). To obtain values for Δ_λ from transfer matrix calculations, the following procedure is applied: For 0° emission angle, the transmission spectrum is calculated depending on the cavity layer thickness ℓ_c . This gives the dependence of $\lambda_m(0^\circ)$ on ℓ_c . Additionally, for $\theta = 30^\circ$, the transmission spectrum is calculated for TE- and TM-polarisation depending on the cavity thickness. This yields $\lambda_m^{\text{TE}}(30^\circ)$ and $\lambda_m^{\text{TM}}(30^\circ)$ depending on ℓ_c . λ_s is always set to 417.5 nm, the average value of the experimental results. From this, it is easily calculated how $\Delta_\lambda(30^\circ) = \lambda_m^{\text{TE}}(30^\circ) - \lambda_m^{\text{TM}}(30^\circ)$ depends on $\Gamma_\lambda = \lambda_m(0^\circ) - \lambda_s(0^\circ)$, since the relation of both quantities to ℓ_c is known. Because the dependence on ℓ_c is monotonous, Δ_λ and Γ_λ may be related to each other. For these calculations the refractive indices obtained from the fitting procedure described above are used.

Figure (4.6) shows the experimental results of the dependence of the polarisation splitting on the detuning, together with the results from corresponding transfer matrix calculations and from direct calculations with the approximate formula (2.38). For the calculations with equation (2.38), the same material parameters as for the transfer matrix calculations are used. ℓ_{DBR} and ω_s are calculated with equations (2.33) and (2.29). The error bars of the measurement results in figure (4.6) in the Δ_λ direction are due to the accuracy in identifying the peaks of the emission lines in the spectrometer images. The errorbars in the Γ_λ direction originate from the accuracy in the fitting procedure used to obtain the λ_s values per measurement. The error in identifying $\lambda_m(0^\circ)$ in the spectrometer images is two orders of magnitude lower (~ 0.4 nm).

The experimental results agree well with the predictions from transfer matrix calculations. Also, the splitting has the same order as predicted by Panzarini et al. [7, 8]. This confirms that the polarisation splitting of the cavity modes of the investigated planar DBR microcavity can be understood within the theoretical framework presented in section 2.6, namely different ℓ_{DBR} and ω_s for TE and TM polarisation and a mismatch of ω_m and ω_s . There is no need to account for other effects like anisotropy, as, for example, Stelitano et al. [17, 18] had to do because they observed five times higher splitting values than predicted by that theory. The material CBP:BSB-Cz (2 wt%) incorporated in the cavity measured in the present work does not exhibit intrinsic anisotropy.

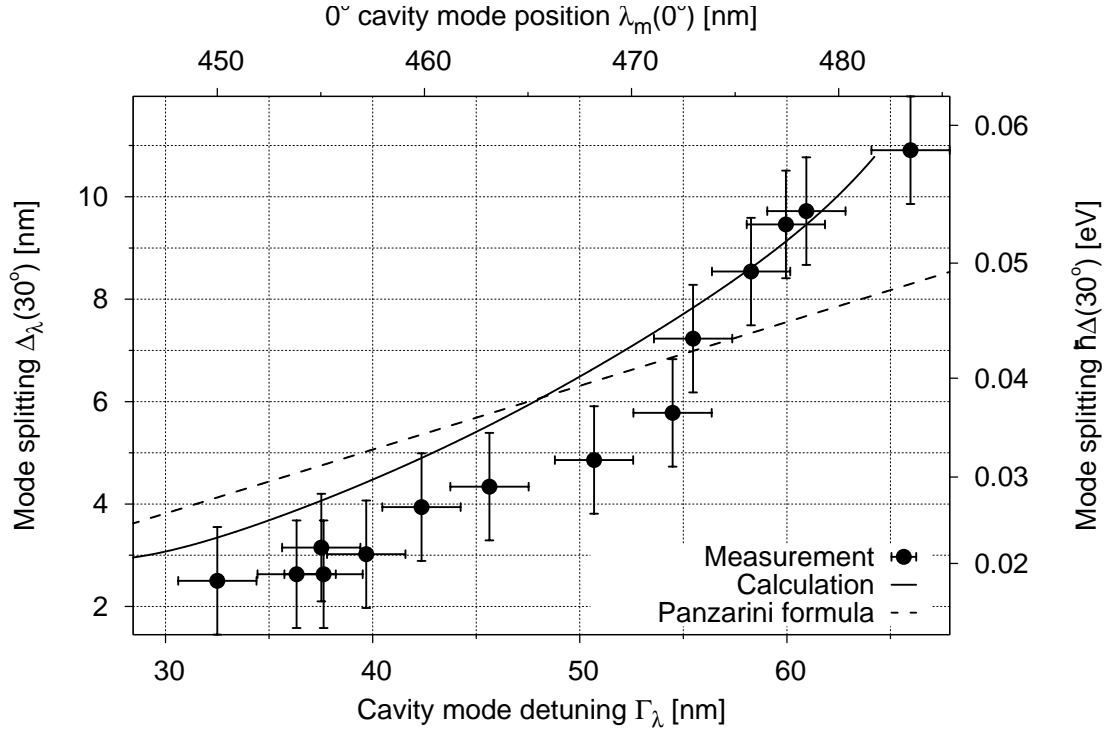


Figure 4.6: Polarisation splitting at 30° emission angle depending on the cavity mode detuning: Measurement results (symbols), transfer matrix calculation (solid line) and approximated theoretical prediction by Panzarini et al. [7, 8] (equation (2.38)) (dashed line). The polarisation splitting is plotted versus detuning. The 0° cavity mode wavelength is only indicated for reference and is for the experimental results only approximately; that is because the centre of the stop band varies from measurement point to measurement point, which gives no definite mapping between Γ_λ and λ_m . For making the $\lambda_m(0^\circ)$ scale, a fixed $\lambda_s(0^\circ) = 417.5$ nm is used.

5 Experimental Proof of spatial Mode Locking in planar Microcavities.

This chapter presents experiments which prove that for excitation with small pumping spots, the radius of the cavity modes exceeds the excited area. Furthermore, phase locking of two spatial cavity modes in the lasing regime is shown. The phase between the two modes is either 0 or π , depending on the distance of the excitation spots.

This chapter consists of three sections. The first section of this chapter describes the sample used. The second section introduces a modification of the experimental setup done in order to get two laser spots for excitation. Furthermore, the way the experiments are conducted is presented. The third section shows the results and their discussion.

5.1 The Sample.

The sample was prepared similarly to the sample described in section 4.1, with some changes. As in section 4.1, the mirrors are DBRs with TiO_2 and SiO_2 as mirror layers with 11 layers of TiO_2 and one layer of SiO_2 between each two TiO_2 layers. Here, the centre of the stop band was chosen to be around $\lambda_s \approx 620 \text{ nm}$. The cavity layer consists of a material different from the previous sample: Aluminium-tris(8-hydroxyquinolin) (Alq_3 , $\text{C}_{27}\text{H}_{18}\text{AlN}_3\text{O}_3$) as host with two weight percent of 4-(dicyanomethylene)-2-methyl-6-(4-(dimethylamino)styryl)-4H-pyran (DCM, $\text{C}_{19}\text{H}_{17}\text{N}_3\text{O}$) (see figure 5.1 for the chemical structures) embedded as dye. Absorption and photoluminescence spectra of these materials are shown in figure 5.2. Both, Alq_3 and DCM, can be excited by absorption of light. If Alq_3 is excited, it transfers its excitation energy via Förster transfer [14] to DCM, which acts as emitter. The cavity layer was designed to have a homogeneous thickness of $\frac{\lambda_s}{2} = 310 \text{ nm}$.

Pure Alq_3 is a favourable material for organic light emitting diodes. It is studied in [21]. DCM is a laser dye, its properties are presented in [22]. Most importantly, it has a

high photoluminescence quantum efficiency combined with a good photostability. Alq_3 is a adequate matrix material for DCM, because the absorption curve of DCM overlaps with the emission curve of Alq_3 (see figure 5.2). This makes it possible to transfer the energy absorbed by Alq_3 to the DCM molecules by Förster energy transfer. These properties make the system Alq_3 :DCM well suited for lasing experiments like the one presented in this work.

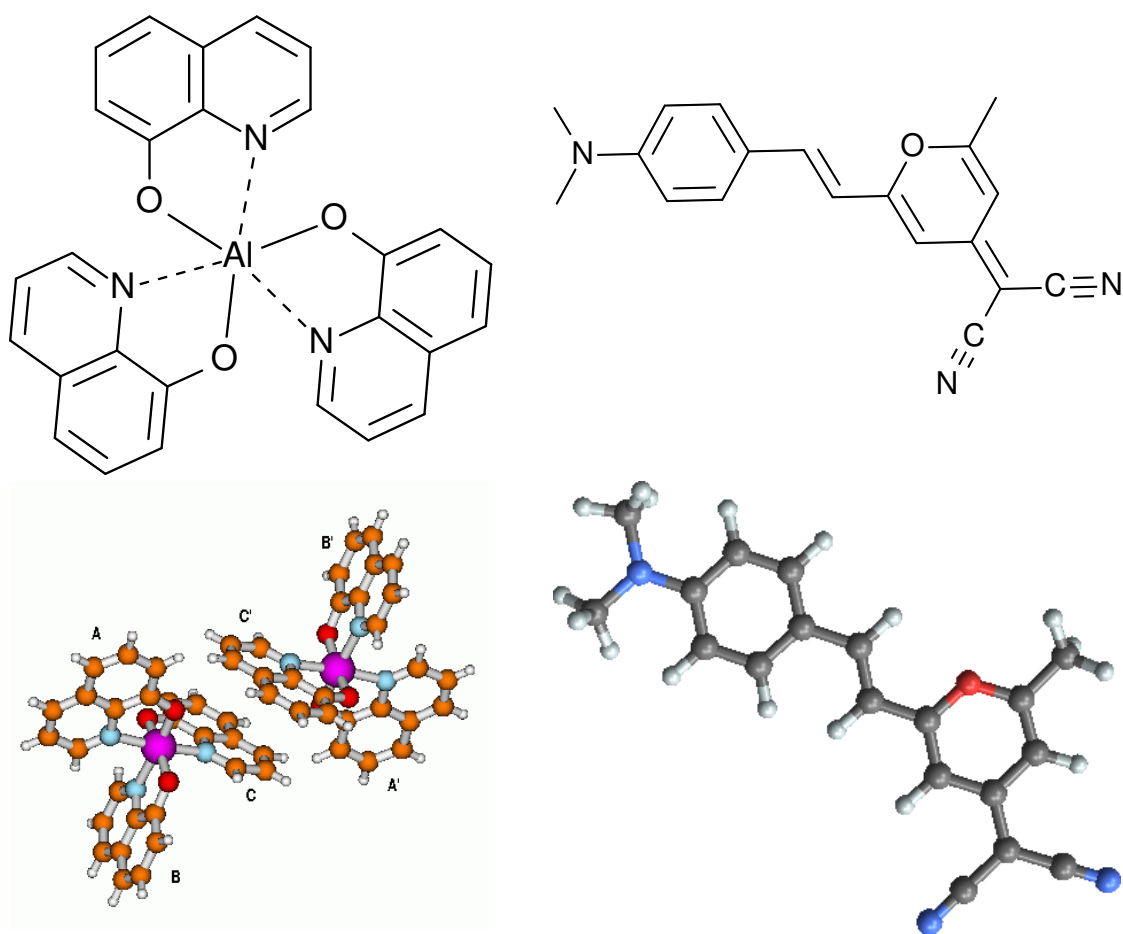


Figure 5.1: Chemical structure of Alq_3 (left) and DCM (right). Schematically (top) and as three dimensional view (bottom). For Alq_3 , the three dimensional view contains two views from different directions. The three dimensional view for Alq_3 is taken from the internet from [19], the one for DCM from the internet from [20] and was vertically mirrored afterwards.

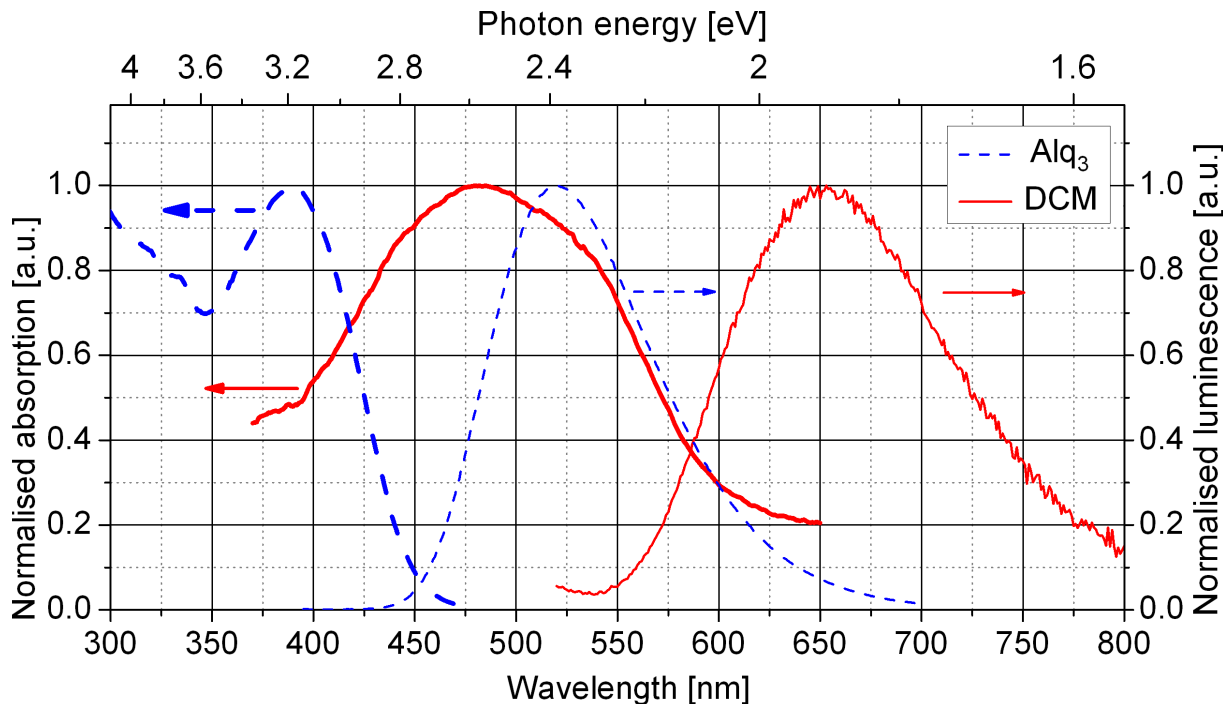


Figure 5.2: Absorption and emission spectra of Alq₃ and DCM. The blue / dashed lines are for Alq₃, the red / solid lines for DCM. The thick lines represent the absorption, the thin lines the luminescence spectra. All spectra are individually normalised to one.

5.2 The Measurement.

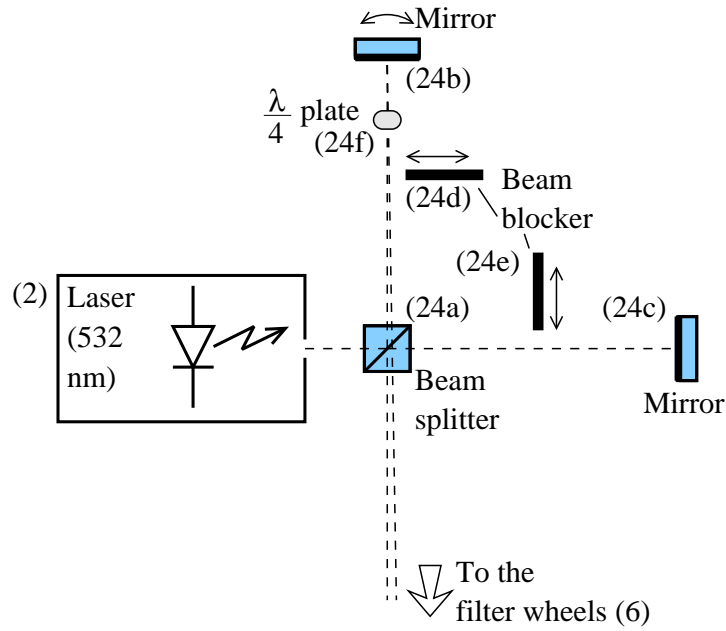


Figure 5.3: Modification of the experimental setup depicted in figure 3.1 with added beam splitter.

For the measurement, the setup described in chapter 3 and depicted in figure 3.1 is used, with a small modification: To get two beams, the mirror (24) in front of the green 532 nm laser (2) is replaced by an arrangement of a beam splitter (24a) and two mirrors (24b) and (24c), see figure 5.3. The distance between the beam splitter and the mirrors is approximately the same. In one light path, a $\frac{\lambda}{4}$ plate (24f) is introduced to turn the polarisation of this light by 90° ⁱ. This is done to avoid interferences between the two beams. The two beams excite the sample at two spots (see figure 5.4). On the sample, the spot centres are separated along the x direction by a distance s . To tune s , mirror (24b) is adjusted along its vertical axis. For excitation at only one spot, it is possible to block one or the other beam with the beam blockers (24d) and (24e).

For excitation, the green laser, operating at a wavelength of 532 nm, is used. With the

ⁱWhen the light passes the $\frac{\lambda}{4}$ plate once, linear polarisation is transformed to circular polarisation. After reflection at the mirror (24b), the light passes the $\frac{\lambda}{4}$ plate a second time, which then renders the originally linear polarised light linear polarised again, but now orthogonally with respect to the previous polarisation direction.

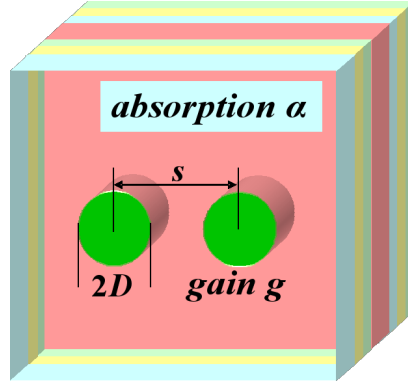


Figure 5.4: Sketch of the geometry of the sample excitation. The microcavity extends to infinity in the x - y -direction. The green circular regions are regions of excitation with a radius D and a distance s between their centres. The background absorption of the cavity material is α and the gain of the excited region g .

filter wheels (6), the excitation power is adjusted. When the sample shows lasing, the intensity emitted into the laser mode and projected onto the spectrometer can get quite high. To avoid saturating or even damaging the CCD detector, additional grey filters (23) are inserted between the sample and the spectrometer as needed. The excitation spot diameter $2D$ is adjusted to be approximately $3\text{ }\mu\text{m}$. With this small spot size, the cavity operates in single spatial mode regime at that spot as depicted in figure 2.13 (a). The intensity of the two excitation beams is approximately the same.

For different spot distances s , the following measurements are carried out:

- Recording of the near field and the far field emission spectrum for one and two excitation spots with different excitation intensities,
- measuring the output intensity depending on the excitation intensity (input-output-curve) for one and two excitation spots.

To reduce degradation of the sample at high intensities, when measuring the input-output-characteristics, the input intensity is not increased further after the system passes the lasing threshold. This input intensity limiting is done because at the same sample position, up to three measurements are conducted: Input-output-behaviour with excitation at spot 1 only, with excitation at spot 2 only, and with excitation simultaneously at spot 1 and spot 2.

When measuring near field and far field emission spectra, the intensities of the spots are adjusted as follows: When the sample is excited by only one spot, the intensity is chosen such that the cavity is operating slightly below lasing threshold. On the other hand, when two spots excite the sample simultaneously, the cavity is in the lasing regime.

Each measurement series is done at a new place on the sample in order to use a virgin, non degraded area. The drawback of this is that, due to fabrication tolerances, the cavity parameters are slightly different for each measurement, making the results only qualitatively comparable.

The measurement of input-output-curves is only supplementary. The aim of this work is to show spatial phase locking of modes. But the recording of input-output-characteristics helps to get an understanding of the degradation of the sample: At the same position, the input-output-curve is recorded several times. Sample degradation can be seen in a shift of the laser threshold towards higher pump energies.

5.3 Results.

The figures 5.5 to 5.10 present spatially and angle resolved emission spectra of the cavity, excited only in spot 1 (subfigure (a)), only in spot 2 (subfigure (b)) or in both (subfigure (c)) spotsⁱⁱ. The distance s between the centres of the spots is ca. $5\text{ }\mu\text{m}$ (figures 5.5 and 5.6), $\approx 6.4\text{ }\mu\text{m}$ (figures 5.7 and 5.8) and about $10\text{ }\mu\text{m}$ (figures 5.9 and 5.10).

It is possible to tune the pump intensity of the excitation beam such that there is no lasing when the sample is excited in only one spot, but it lases when the excitation is performed in both spots. The lasing transition is visible from the spectrograms (figures 5.5 to 5.10): Under two spot excitation, the emission maximum is spectrally much sharper (the measured data shows a width of approximately 0.75 nm of the lasing modes, which is the resolution limit of the experimental setup) and one to two orders of magnitude higher compared to the excitation with only one beam.

This is understood as follows, assuming that the pump spot radius D is smaller than the cavity mode radius d : The cavity modes associated with the pump spots spatially exceed the excited regions and overlap with each other. In this way, photons from mode 1 can stimulate emission in the excited region corresponding to mode 2. This induces

ⁱⁱThe numbering of the two spots is arbitrary.

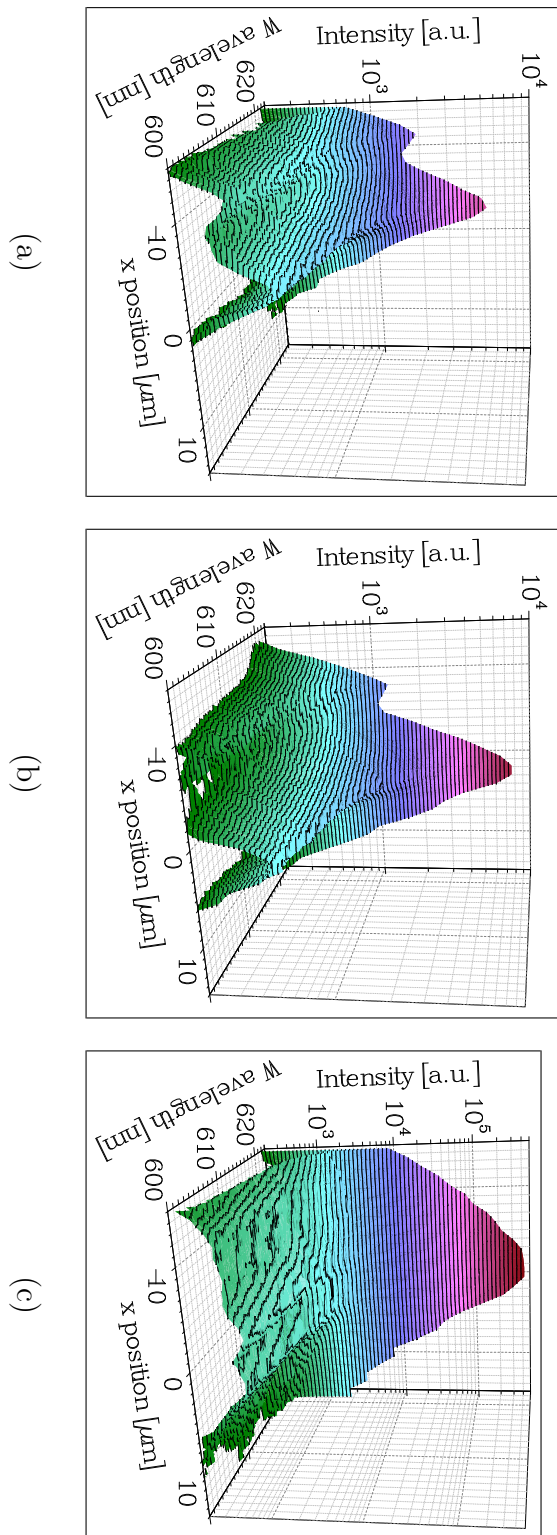


Figure 5.5: Spatial resolved emission spectra for $\approx 5 \mu\text{m}$ spot distance. (a): Excitation at the left spot only. (b): Excitation at the right spot only. (c): Excitation at both spots. In (c), the one broad supermode which forms above lasing threshold is clearly discernible.

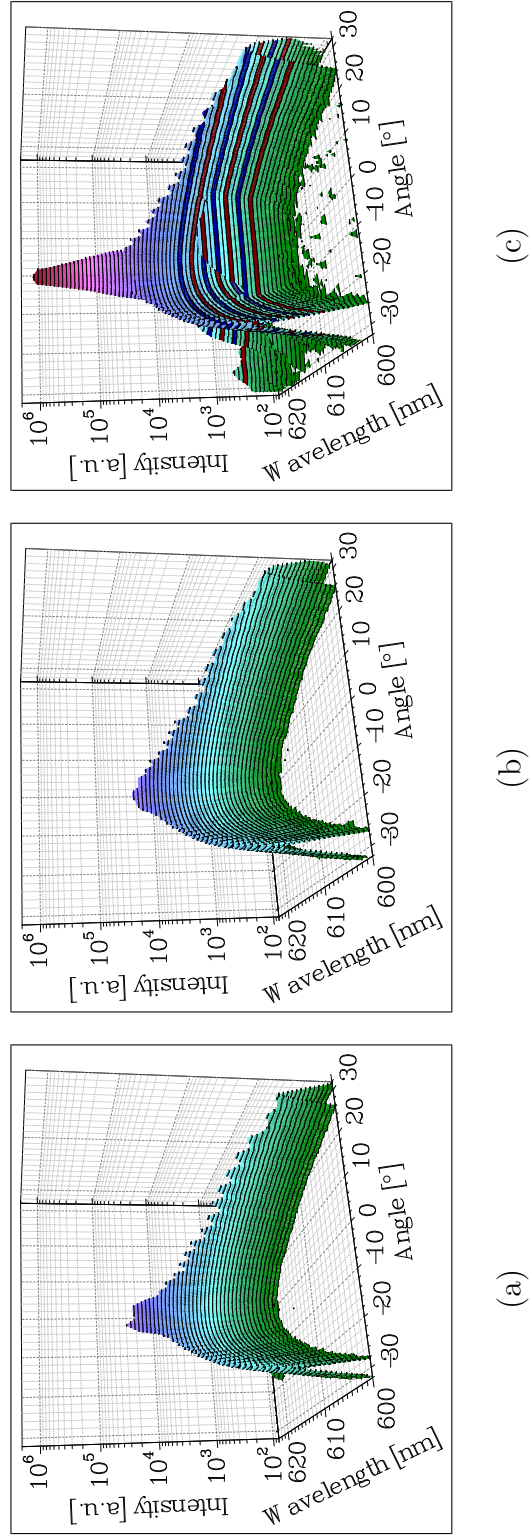


Figure 5.6: Angle resolved emission spectra for $\approx 5 \mu\text{m}$ spot distance. (a): Excitation at the left spot only. (b): Excitation at the right spot only. (c): Excitation at both spots.

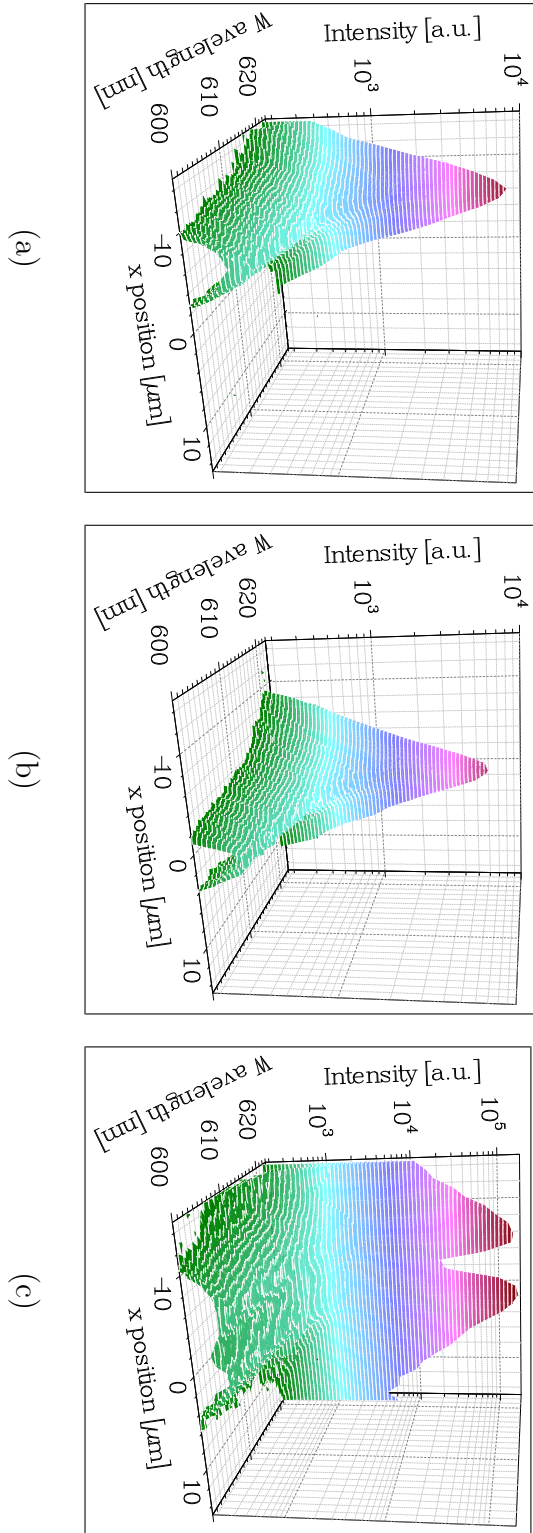


Figure 5.7: Spatial resolved emission images for $\approx 6.4 \mu\text{m}$ spot distance. (a): Excitation at the left spot only. (b): Excitation at the right spot only. (c): Excitation at both spots. In (c), note the higher steepness of the intensity fall off between the emission peaks compared to its value outside.

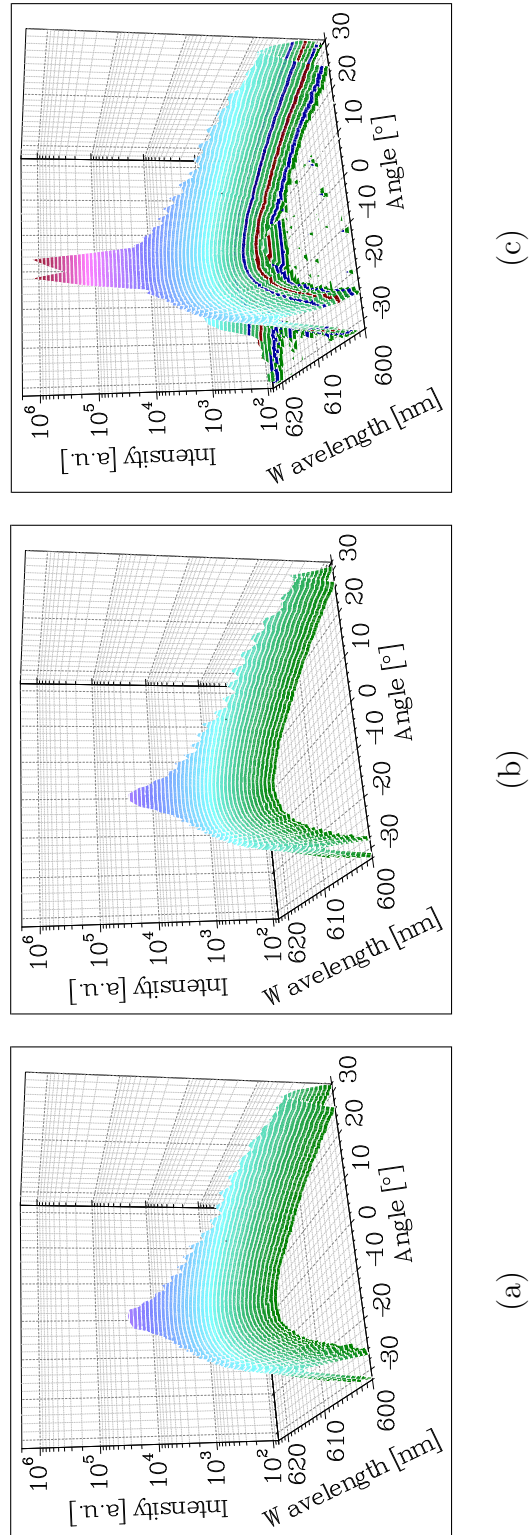


Figure 5.8: Angle resolved emission images for $\approx 6.4 \mu\text{m}$ spot distance. (a): Excitation at the left spot only. (b): Excitation at the right spot only. (c): Excitation at both spots. Note the emission into oblique directions in (c).

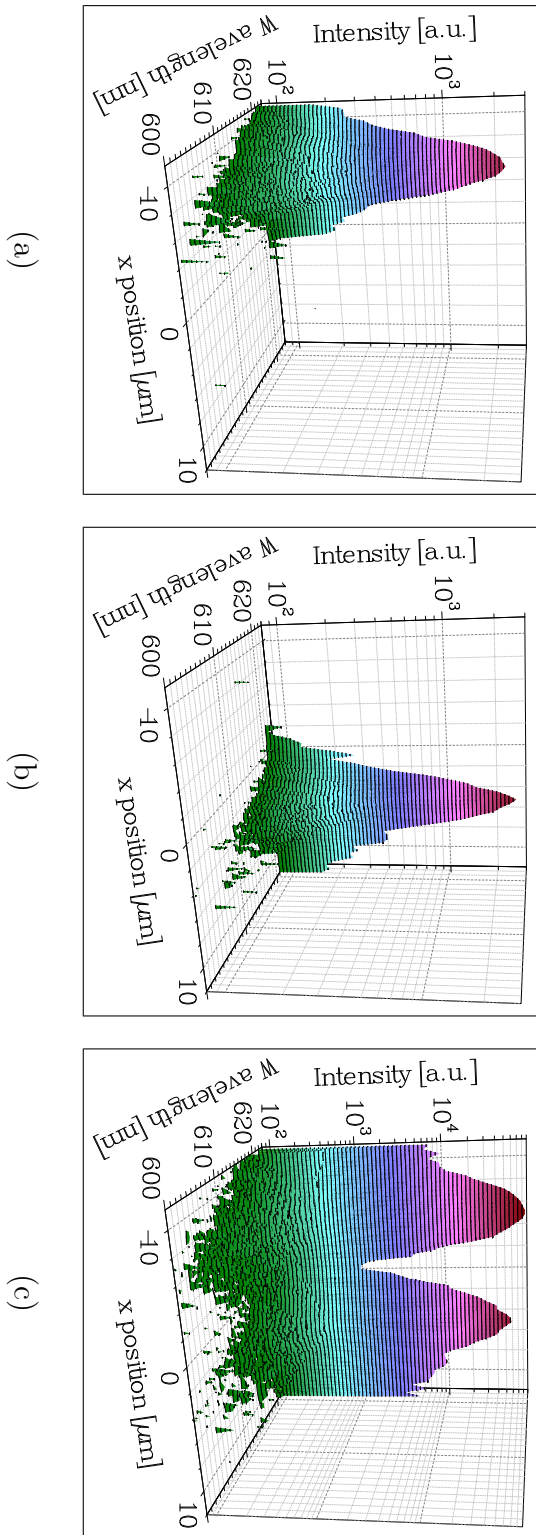


Figure 5.9: Spatial resolved emission images for $\approx 10 \mu\text{m}$ spot distance. (a): Excitation at the left spot only. (b): Excitation at the right spot only. (c): Excitation at both spots. In (c), note the low intensity between the spots.

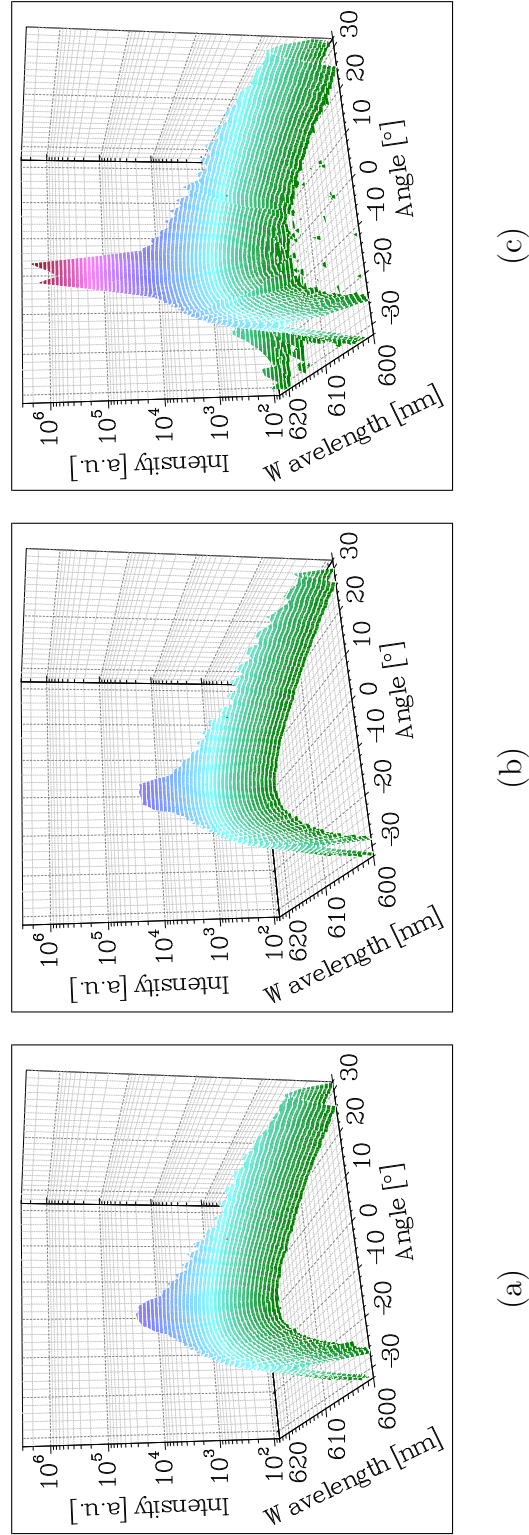


Figure 5.10: Angle resolved emission images for $\approx 10 \mu\text{m}$ spot distance. (a): Excitation at the left spot only. (b): Excitation at the right spot only. (c): Excitation at both spots. In (c), note the emission into oblique directions.

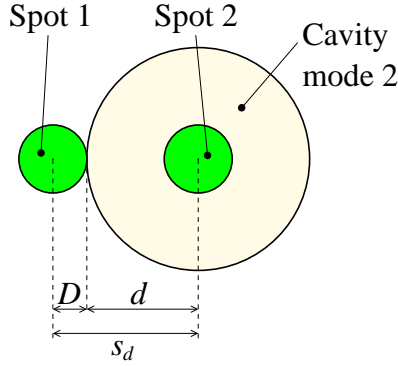


Figure 5.11: Illustration of a way to qualitatively determine the mode radius d . The distance s_d between the two excitation spots is the distance, at which the effect of lowered lasing threshold when exciting with two spots instead of one just disappears for increasing s . To aid clarity, only one cavity mode is shown.

slightly more photons in mode 2, which in turn slightly increase the stimulated emission in mode 1, and vice versa. If the system, excited with only one spot, is close enough to the lasing transition, the increased stimulated emission when switching on the second spot then drives the cavity through the lasing transition. The two modes are coupled by this stimulated emission.

The distance s_d between the two excitation spots at which this coupling and cross-stimulation effect is no longer observed can be qualitatively related to the radius d of the modes as follows:

$$d \sim s_d - D \quad (5.1)$$

(See figure 5.11). Of course, this relation is only qualitative, since it assumes a spatially homogeneous excitation across the pumped area and a cavity mode with homogeneous field strength along the x - y -direction within the mode radius. However, this formula gives a very rough estimation for the mode radius.

In the case of s being about $5 \mu\text{m}$, and when exciting at two spots, the laser emission is spatially broadly distributed with its maximum *between* the excited regions (see figure 5.5). In the angular distribution, the emission is fairly narrowly peaked around the forward direction ($\theta = 0^\circ$, see figure 5.6).

For a higher distance between the excitation spots, $s \approx 6.4 \mu\text{m}$, the situation is quite different: The laser emission spatially originates from the regions where the sample is

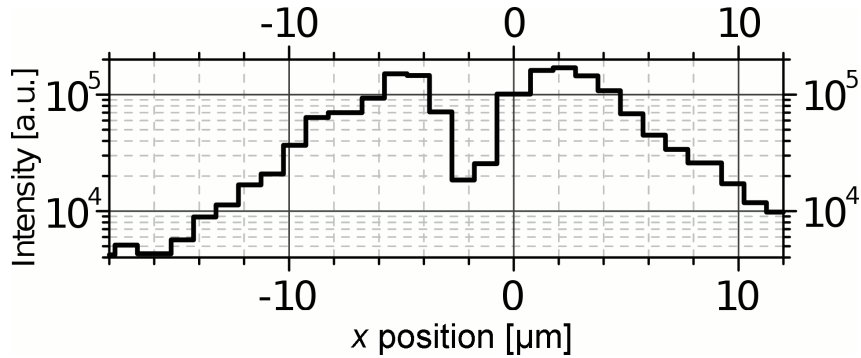


Figure 5.12: Spatial cross section through the data of figure 5.7 (c) at the wavelength of maximal intensity (621.5 nm).

excited and not from in between (see figure 5.7). The light is emitted into two symmetrically oblique directions ($\theta \approx \pm 2.5^\circ$, see figure 5.8), whereas the emission below lasing threshold is symmetrically distributed around $\theta = 0^\circ$. Also important to mention is that in the spatially resolved spectrum, the intensity falls off *between* the emitting spots much steeper than outside: Inside, to ca. 0.1 of the maximum intensity over around $3.5 \mu\text{m}$, outside, it needs ca. $7 \mu\text{m}$ for the same fall off. It is not possible to extract precise values for the intensity slope between the two maxima because they are only seven pixels apart. Only three to four pixels separate the maxima from the dip in between. Additionally, the maxima are approximately two to three pixels wide, so that at the end the falloff from the maxima to the dip is within two to three pixels. This does not allow for a good steepness calculation. In fact, it can be assumed that, in reality, the intensity between the two spots is much lower than the minimum intensity in the spectrometer image, which is so “high” due to the limited resolution. Figure 5.12 shows a cross sectional plot along the x direction of the emission for the wavelength of maximum intensity (621.5 nm).

For $s \approx 10 \mu\text{m}$, the results are qualitatively the same as for $s \approx 6.4 \mu\text{m}$. Also here the laser emission takes place in a direction of $\theta \approx 2.5^\circ$. Note, that in both cases in the spectrometer image the distance between the angular maxima is only a few pixels (between three and four). This resolution does not yield precise values for the angles of maximum emission.

Lastly, it is noted that, when the sample is excited with two pump beams and the intensity is lowered such that the sample does not show lasing, the spatial emission is like the sum of the spatial emissions in the case when the sample is excited at only the one

and only the other spot individually. Furthermore, the angle resolved emission in this case is the same as when the sample is excited at only one spot. This is true for all investigated values of s . Only above lasing threshold, the emission pattern changes into a) a spatially broad emission centred between the spots and peaked around the normal direction, or b) an emission with minimised intensity between the spots, and the angular pattern to one with two oblique peaks.

Interpretation of the Results.

The results can be understood in the following way: When the cavity is operating in the regime of spontaneous emission, each optically active molecule in the cavity emits (almost) independently from all the others; the emission is incoherent. Therefore, in this regime, if the sample is excited at two spots, the intensity of the emitted light is just the sum of the intensities of the emission when the sample is individually excited at the one or at the other spot.

If the excitation intensity is chosen such that the sample shows lasing when it is excited at two spots but no lasing when pumped at only one position, the situation is the following: Photons emitted from spot 1 stimulate emission of other photons inside spot 1, but also to some extent inside spot 2. These photons emitted from spot 2 react back to spot 1 by stimulating the emission of further photons thereⁱⁱⁱ. This small additional stimulation, compared to the case of pumping at only one spot, can make the difference needed to start lasing. Since the spontaneous emission couples, the emission from both spots is (partly) coupled and mutually coherent. So, the intensities of the light emitted from both spots can no longer be added, instead, the amplitudes have to be added, making interference possible.

In the case of $s \approx 5 \mu\text{m}$ (figures 5.5 and 5.6), both spots emit with the same phase (phase difference ϕ between both spots zero). That is why both spots form one big *superspot* and emit in the forward direction $\theta = 0^\circ$.

The cases of $s \approx 6.5 \mu\text{m}$ and $s \approx 10 \mu\text{m}$ can be interpreted with the assumption that the excited regions are phase locked with a relative phase ϕ of $\phi = \pi$. This gives an antisymmetric distribution of the electromagnetic field amplitude. However, since the

ⁱⁱⁱOf course, photons emitted from spot 2 stimulate much more further photons from spot 2 than from spot 1.

geometry of the excitation is symmetric, the emission has to be zero between the two spots. Coherent emission from two spots with a phase difference not equal zero dictates that the emission maxima are not in the normal direction. For $\phi = \pi$, the emission maxima are symmetric around $\theta = 0^\circ$, and in normal direction there is no emission. This can easily be understood with the same symmetry argument used above. Rigorously, if one calculates the interference pattern of two equal coherent emitters with a phase difference of π between them, an emission minimum will be in the forward direction where there is destructive interference of the light emitted from the two spots.

Input-Output-Curves.

For completeness, figure 5.13 shows the measured input-output-curves for two different distances between the emission spots, namely $s \approx 8.5 \mu\text{m}$ and $s \approx 12.25 \mu\text{m}$. The input-output-characteristics show that the lasing does set on a bit earlier when the sample is excited with two beams, compared to the case of excitation at only one spot. For $s \approx 8.5 \mu\text{m}$, the excitation energy at the onset of the laser transition is around 2 times larger for one spot excitation compared to the case of two spot excitation. For $s \approx 12.25 \mu\text{m}$, this factor is about 1.5. This difference in the laser threshold should depend on the spot distance: It should be larger for smaller s because the spatial mode coupling is bigger when they overlap more. This is not violated in these measurements, but since there are input-output-curves for only two different values of s , nothing more can be said about this. To get a rough feeling for the degradation of the sample, for $s \approx 8.5 \mu\text{m}$ the measurement of the input-output-behaviour at two spot excitation is done twice: Once at the beginning, once after measuring the curves for excitation at spot 1 and at spot 2 individually. The second measurement shows the lasing onset a bit later than the first one, but it is still earlier than the onset at excitation with only one beam: About 1.5 times the excitation energy is needed in the second measurement. This shows that the sample degrades while the measurement is in progress, but not so much to make the results useless.

Discussion.

The experiments demonstrate that the lasing mode can spatially extend beyond the region where there is gain. They also demonstrate a phase locking and supermode formation of individual spatial modes in the lasing regime. The fact that the lasing mode can be

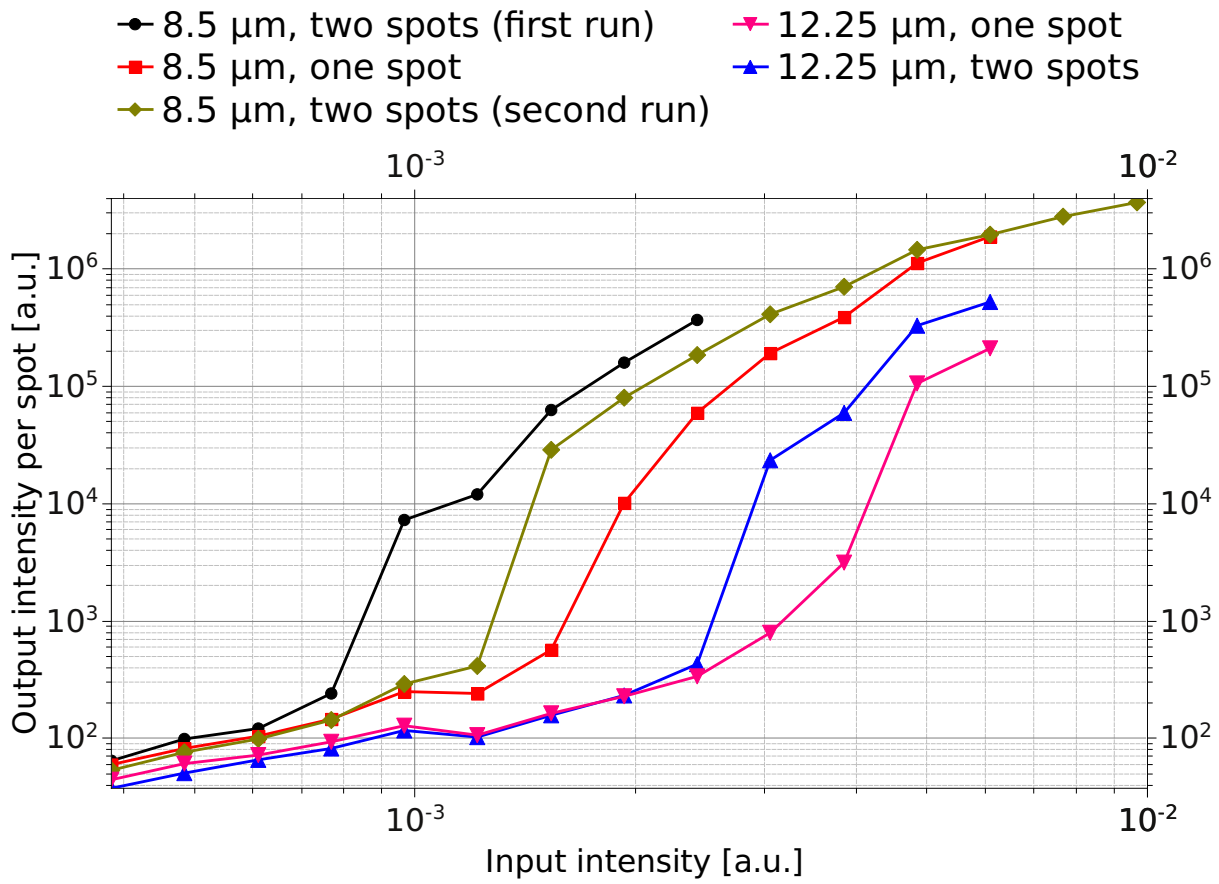


Figure 5.13: Input-output-curves for excitation with one beam and two beams for two different values of the distance s between the excited spots. For $s \approx 8.5 \mu\text{m}$, one measurement was carried out twice (see text).

broader than the excited area is important from the application point of view, because outside the excited area there is no gain and so the electromagnetic field will be damped. For constructing a laser with minimised pumping intensity, which is desirable especially for an electrically pumped organic laser due to the material degradation at higher energy densities, it is therefore important to excite a broad region, so that the lasing mode is overlapping as much as possible with regions where there is gain.

Numerical calculations have been done by another member of the research group of this work. They reproduce the experimental results laid out in this chapter. The calculations were done with a commercial software which solves Maxwell's equations in a simplified framework. The results from this calculations show similar angular and spatial emission spectra as the experiments.

6 Conclusion and Outlook.

6.1 Conclusion.

This work consists of two parts. In the first part, the effect of mode tuning on the cavity mode polarisation splitting was studied, experimentally and theoretically. The organic host-dye-system CBP:BSB-Cz (2 wt%) was used as active medium, while distributed Bragg reflectors formed the mirrors of the microcavity. The measured sample had a wedge shaped cavity layer which made it possible to change the spectral cavity mode position within the stop band by varying the measurement position on the sample.

In the experiment, polarised angle resolved emission spectra from this system were recorded at different sample positions. Corresponding calculations, utilising the transfer matrix method, were conducted. At angles different from zero, a splitting of the cavity resonant mode into two modes could be observed, and it could be shown that these modes are orthogonally polarised. The splitting of the modes did increase with the angle of emission and with the detuning of the cavity mode with respect to the DBR stop band. The experimental results agreed with the corresponding transfer matrix calculations and approximate analytical calculations.

The effect of polarisation splitting in the studied DBR microcavities could be understood due to the following effects: The polarisation dependence of the penetration depth of light into the DBR, the polarisation dependence of the centre frequency of the DBR stop band, and the mismatch of the cavity mode frequency and the frequency of the stop band centre. In particular, there was no need to account for material anisotropies.

The second part presented considerations about the in plane size of cavity modes and about phase locking of different spatial modes. Here, Alq₃:DCM (2 wt%) was used as the active medium in the measured microcavity. The sample was excited at two small spots, about 3 μm in diameter, which were a few μm apart. Excitation at only one of these spots was also performed.

In the experiment, the excitation energy was chosen such that the sample showed lasing when it was pumped at both places. However, the laser emission vanished when only one spot was excited. Depending on the distance between the spots, the laser emission from both spots turned out to either propagate in forward direction and originate from one broad area, extending over both spots and the space in between, or to propagate in oblique direction and originate sharply peaked at the two excitation spots with minimised intensity in between.

The results indicated that the cavity modes were larger than the pump spots, and that the mode associated with one spot did overlap with the other spot, respectively. Via this overlap, the emission from one spot could stimulate emission in the other spot and vice versa. Both modes coupled via stimulated emission, and they locked their phases. The phase difference was 0 in the case of normal emission and π in the case of oblique emission.

6.2 Outlook.

The values of polarisation splitting in detuned organic microcavities presented in this work ranged up to 58 meV, which corresponds to a photon frequency of 14 THz. However, THz radiation can not directly be produced by this devices because the split up modes are orthogonally polarised and hence do not mix. With appropriate mixing device, it could be possible to generate electromagnetic THz radiation utilising the presented polarisation splitting effect.

For constructing an electrically pumped organic laser, the main obstacle is the low electron mobility in organic semiconductors. This leads to a high electric pump intensity needed to start lasing. This intensity would destroy the organics immediately. Therefore, it is of interest to reduce the pump intensity needed to start lasing. Furthermore, electric contacts on the cavity are a good absorber for light, so it is desirable to have no contacts where the laser light escapes. Hence, one important step towards an electrically pumped organic laser is, besides lowering the laser threshold, to find optimal excitation geometries.

The results presented in this work show that the lasing mode has a spatial extent of $> 10 \mu\text{m}$ in the cavity plane. Therefore, an interesting experiment would be to excite the sample with one spot of variable diameter and measure the energy needed to get lasing depending on the spot size. One thesis is, that, starting from very small spot sizes, the energy for the lasing threshold first decreases as the spot does more and more overlap with

the cavity mode, and then increases again as the spot gets larger than the lasing mode. This is subject to further investigations.

For a quantitative measurement of the spatial extension of cavity modes, the technique of carefully measuring the input-output-characteristics for varying s for one and two spot excitation can be used. The idea is that the overlap of the cavity modes manifests in a shift of the laser threshold to lower pump intensities. A first experiment of this kind was done by De Martini et al. [11] in 1990.

Another direction to conduct research is structuring of electrodes for electrical pumping. It could be interesting to study ring electrodes with a radius approximately the same, or a bit smaller, than the cavity mode radius. The idea is to find a compromise between good excitation of one cavity mode and avoiding of absorption by electrodes.

Referring to work done by Langner et al. [23, 24], if the cavity is structured in the x - y -plane, the cavity modes get spatially discretised, and can have shapes with several minima and maxima of intensity along the x - y -direction. Furthermore, the lasing threshold is lowered in that case because the light is also confined in the lateral direction. For these systems, it is interesting to investigate electrodes placed at the minima of the desired cavity mode.

From the point of fundamental physics, it is interesting to try to understand the results on spatial mode locking presented in this work in terms of polariton condensates. Many articles in literature, for example [25] by Lai et al. and [26] by Wouters et al., present similar results in inorganic microcavities and explain it in terms of Bose-Einstein-condensation of cavity polaritons.

Appendix.

Publications.

During this diploma thesis, the article [27] was published in a peer reviewed journal.

A poster showing the main results of this work was shown at an interdisciplinary congress [28].

List of Symbols.

Symbol:	Meaning:
\vec{E}	Electric field vector.
\vec{B}	Magnetic field vector.
\vec{E}_0	Electromagnetic wave electric field amplitude.
\vec{A}	Electromagnetic wave electric field complex amplitude.
R	Right propagating Electromagnetic wave electric field complex amplitude.
L	Left propagating Electromagnetic wave electric field complex amplitude.
I	Intensity.
P	Power.
ω	Angular frequency.
λ	Wavelength.
\vec{k}	Wave vector.
\vec{s}	Unit vector in direction of the wave vector.
t	Time. Electric amplitude transmission coefficient.
r	Electric amplitude reflection coefficient.
τ	Life time.
\vec{r}	Coordinate vector.

x, y, z	Cartesian coordinates.
θ	Angle.
ϕ	Phase.
δ	Relative phase; phase shift.
n	Refractive index.
μ_r	Relative magnetic permeability.
c	Speed of light in vacuum.
\hbar	Reduced Planck constant.
\mathcal{R}	Power reflectance.
\Re	Modulus of the power reflectance of a DBR.
\mathcal{T}	Power transmittance.
F	Finesse coefficient.
$\bar{r}, \bar{R}, \bar{\Re}, \bar{F}$	Effective (gain and loss compensated) reflectances and finesse.
\mathbf{M}	Transfer matrix.
ℓ	Thickness.
m	Mode order.
index _m	Cavity resonant mode.
index _s	Centre of DBR stop band.
index _c	Cavity layer.
N	Number of layer pairs in a DBR.
Δ	Polarisation splitting. Also used as a radical to form uncertainty quantities.
Γ	Cavity mode detuning.
α	Absorption constant.
g	Gain constant.
$\bar{\alpha}$	Effective (gain compensated) absorption constant.
β	Spontaneous emission coupling factor.
D	Pump spot radius.
d	Cavity mode radius.
s	Distance between excitation spots.
a, b, j	Integer index.
i	Integer index or imaginary unit.

Bibliography.

- [1] Die Schildbürger, published on the websites of *Internet-Märchen*. <http://www.internet-maerchen.de/maerchen/schild00.htm>, November 2009.
- [2] Max Born and Emil Wolf. *Principles of Optics*. Pergamon Press, Oxford, United Kingdom, 6 edition, 1993.
- [3] Bernd Schütte. Lasing characteristics of optically structured organic microcavities, diploma thesis at the *Technische Universität Dresden*, Germany, 2008.
- [4] E. M. Purcell. Spontaneous emission probabilities at radio frequencies. *Phys. Rev.*, 69:681, 1946.
- [5] B. E. Sernelius. Lecture notes on “Electrodynamics”, part 13, Linköpings universitet, Sweden. <http://www.ifm.liu.se/~boser/elma/Lect13.pdf>, August 2009.
- [6] *FilmWizard, version 8.1.7*. Scientific Computing International, Carlsbad, CA, United States of America.
- [7] G. Panzarini, L. C. Andreani, A. Armitage, D. Baxter, M. S. Skolnick, V. N. Astratov, J. S. Roberts, A. V. Kavokin, M. R. Vladimirova, and M. A. Kaliteevski. Cavity-polariton dispersion and polarization splitting in single and coupled semiconductor microcavities. *Физика твердого тела*, 41:1223 – 1238, 1999.
- [8] G. Panzarini, L. C. Andreani, A. Armitage, D. Baxter, M. S. Skolnik, V. N. Astratov, J. S. Roberts, Alexey V. Kavokin, Maria R. Vladimirova, and M. A. Kaliteevski. Exciton-light coupling in single and coupled semiconductor microcavities: Polariton dispersion and polarization splitting. *Phys. Rev. B*, 59:5082 – 5089, 1999.
- [9] T. Enomoto, T. Sasaki, K. Sekiguchi, Y. Okada, and K. Ujihara. Intensity fluctuation of a pulsed planar microcavity laser. *Journal of Applied Physics*, 80:6595 – 6601, 1996.

-
- [10] G. Björk, H. Heitmann, and Y. Yamamoto. Spontaneous-emission coupling factor and mode characteristics of planar dielectric microcavity lasers. *Phys. Rev. A*, 47: 4451 – 4463, 1993.
- [11] F. De Martini, M. Marrocco, and D. Murra. Transverse quantum correlations in the active microscopic cavity. *Phys. Rev. Lett.*, 65:1853 – 1856, 1990.
- [12] K. Ujihara. Spontaneous emission and the concept of effective area in a very short optical cavity with plane-parallel dielectric mirrors. *Japanese Journal of Applied Physics*, 30:L 901 – L 903, 1991.
- [13] *WinSpec/32, version 2.5.15.2*. Roper Scientific GmbH Germany, Ottobrunn, Germany.
- [14] T. Förster. Zwischenmolekulare energiewanderung und fluoreszenz. *Ann. Physik*, 1 - 2:55, 1948.
- [15] T. Aimono, Y. Kawamura, K. Goushi, H. Yamamoto, H. Sasabe, and C. Adachi. 100% fluorescence efficiency of 4,4 ‘-bis[(n-carbazole)styryl]biphenyl in a solid film and the very low amplified spontaneous emission threshold. *Appl. Phys. Lett.*, 86, 2005.
- [16] *Film Wizard Getting Started Manual, professional version*. Scientific Computing International, Carlsbad, CA, United States of America, 1994.
- [17] S. Stelitano, G. De Luca, S. Savasta, and S. Patané. Polarized emission from high quality microcavity based on active organic layered domains. *Applied Physics Letters*, 93:193302, 2008.
- [18] S. Stelitano, S. Savasta, S. Patané, G. De Luca, and L. Monsù Scolaro. Origin of giant polarization splitting in high quality organic microcavities. *Journal of Applied Physics*, 106:033102, 2009.
- [19] Website of the *Istituto per la Sintesi Organica e la Fotoreattività*, Molecular Photoscience Group. http://www.isof.cnr.it/photoscience/Alessandra.Degli_Esposti/research.html, November 2009.
- [20] Online service Wolfram|Alpha by *Wolfram Research*. <http://www09.wolframalpha.com/input/?i=DCM>, November 2009.

-
- [21] M. Knupfer, H. Peisert, and T. Schwieger. Band-gap and correlation effects in the organic semiconductor Alq₃. *Phys. Rev. B*, 65:033204, 2002.
- [22] P. R. Hammond. Laser dye dcm, its spectral properties, synthesis and comparison with other dyes in the red. *Optics Communications*, 29:331, 1979.
- [23] M. Langner, R. Gehlhaar, S. I. Hintschich, H. Fröb, H. Wendrock, V. G. Lyssenko, and K. Leo. Optical modes in wavelength-sized organic microcavity structures. *Opt. Quant. Electron.*, 40:403 – 409, 2008.
- [24] M. Langner, M. Sudzius, S. I. Hintschich, H. Fröb, V. G. Lyssenko, and K. Leo. Sub-nanojule threshold lasing in $5 \times 5 \mu\text{m}^2$ organic photonic boxes. *Proceedings of SPIE*, 6999:699902, 2008.
- [25] C. W. Lai, N. Y. Kim, S. Utsunomiya, G. Roumpos, H. Deng, M. D. Fraser, T. Byrnes, P. Recher, N. Kumada, T. Fujisawa, and Y. Yamamoto. Coherent zero-state and π -state in an exciton-polariton condensate array. *nature*, 450:529 – 533, 2007.
- [26] M. Wouters, I. Carusotto, and C. Ciuti. Spatial and spectral shape of inhomogeneous nonequilibrium exciton-polariton condensates. *Phys. Rev. B*, 77:115340–1 – 115340–7, 2008.
- [27] F. Becker, M. Langner, H. Fröb, V. G. Lyssenko, K. Leo, and C. Adachi. Dependence of polarization splitting on mode tuning in microcavities. *Applied Physics Letters*, 95: 191106, 2009.
- [28] MinD Hochschul Netzwerk. MinD-Akademie 2009. <http://mind-akademie.de/>, October 2009.

Acknowledgements.

I would like to express my gratitude to all people who did support me—directly or indirectly—during my diploma thesis. Some of them—without pretending to give an exhaustive list—are specially mentioned below.

In the first place, I like to thank Prof. Dr. Karl Leo for the opportunity to work in the field of lasing. His style of leading the institute makes the work at the Institut für Angewandte Photophysik inspiring.

I express my thank to Prof. Dr. Vadim G. Lyssenko who was my supervisor during my diploma year. Although we had different opinions on some details, I learnt a lot from his inventive way of understanding physics.

I thank Maik Langner and Robert Brückner from the Spex group who did prepare the samples which I was using.

My thanks to Susanne Hintschich, the leader of the Spex group. Even though she was not at the institute for the majority of my diploma time, I especially thank her for her extensive remarks on my written thesis.

The members of the choir of the IAPP also deserve my gratitude. It is always a pleasure for me to sing with this interesting group.

I thank Leslie Lamport for LaTeX, Guido van Rossum for Python and the GNU and BSD projects for gnuplot and many other small useful tools.

My thank to my flatmate Holger Hauptmann with whom it is uncomplicated to live with and who has always an open mind for fundamental discussions.

I want to thank my parents for giving me this life and for moral support during my thesis.

Abschlussklärung.

Hiermit erkläre ich, dass ich die von mir am heutigen Tage dem Prüfungsausschuss der Fachrichtung Physik der Technische Universität Dresden eingereichte Diplomarbeit zum Thema

Polarisation splitting, moderadius and spatial mode locking in planar organic DBR microcavities.

ohne unzulässige Hilfe Dritter und ohne die Benutzung anderer als der angegebenen Hilfsmittel selbständig angefertigt habe. Die aus fremden Quellen direkt oder indirekt übernommenen Gedanken sind als solche kenntlich gemacht. Die Arbeit wurde bisher in gleicher oder ähnlicher Form keiner anderen Prüfungsbehörde vorgelegt, weder im In- noch im Ausland.

Dresden, den 30. November 2009.

Felix Becker.